Engineering Failure Analysis 163 (2024) 108385

Contents lists available at ScienceDirect

Engineering Failure Analysis

journal homepage: www.elsevier.com/locate/engfailanal

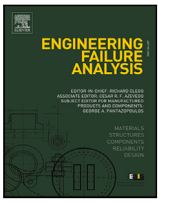

Mapping the defect acceptance for dynamically loaded components by exploiting DIC-based full-field receptances

Alessandro Zanarini

Dynamics & Vibrations of Machines, DIN - Industrial Engineering Department, University of Bologna, Italy

ARTICLE INFO

Keywords:
Defect acceptance
DIC-based dynamic testing
Full-field FRFs
Fatigue spectral methods
NDT

ABSTRACT

Potential defect acceptance can be seen dependable upon the mapping of effective strains on the whole surface, due to dynamic loading of the components as they are mounted. With proper constitutive models and loading spectra, the experiment-based mapping of the equivalent stresses can be achieved from optical full-field receptances in an extremely dense grid, also for lightweight parts, without inertia distortions thanks to contactless measurements. Fatigue spectral methods turn this mapping into components' life distributions, for a clear assessment of the material's utilisation: a risk grading mapping for potential defects can be formulated in the area of inquiry in order to discriminate between safe and dangerous locations. By following this experiment-based approach, potential defects in exercise and production might be tolerated in safer locations, under the chosen dynamic task, with great savings in costs and maintenance. Among the image-based full-field measurement techniques, Hi-Speed DIC has proved to work in many environments, to be able to estimate full-field receptances of real components in their effective assembling and loading conditions, in different cases of industrial interest. The quality achieved by DIC in the receptance maps helps in numerically deriving the strain FRFs on the sensed surface. Extended scenarios – with newly modelled coloured noises for an advanced excitation definition from two shakers – and a vibrating rectangular plate, as real mounted component, are highlighted in details to prove the effectiveness of DIC-based risk index mapping under defect acceptance criteria.

1. Introduction

The key idea sketched in this extended article is to use DIC-based optical full-field FRF datasets, in their native resolutions in frequency and spatial domains, to bring the complete and real structural dynamics into fatigue life expectations for risk mapping, once advanced excitation modelling is adopted. Using datasets in native resolutions means without any interpolation error from reductions or topological transforms, therefore maximising the quality of derivative operations as in [1]. A risk index mapping is built, based upon component life estimations in the whole sensed area: this can highlight where a potential defect in operation might be dangerous or not. All this finely mapped failure knowledge enriches a risk tolerance strategy of the defects that may be anywhere inside the parts, due to the manufacturing/mounting process or to excessive loading during service. Briefly introduced in [2] by means of reduced DIC-based datasets, the broad frequency band *experiment-based optical full-field FRF approach* is here deployed at maximal level with native resolution *receptances* [3,4] by high-speed DIC, instead of reduced datasets by stroboscopic ESPI as in [1,5–8]. An overview of the approach is sketched in Fig. 1, with the aid of the math later introduced. The *experiment-based optical full-field FRF risk mapping approach* brings threefold advantages. First: it inherits the real structure directly from testing, without

E-mail address: a.zanarini@unibo.it.
URL: https://www.colorazeta.it/EngResearch/Zanarini_index_EN.htm.

https://doi.org/10.1016/j.engfailanal.2024.108385
Received 31 January 2024; Received in revised form 29 April 2024; Accepted 30 April 2024
Available online 9 May 2024

Abbreviations

DIC	Digital Image Correlation	(ω)	Frequency dependency
dof	Degree of freedom	$F(\omega)$	Excitation force
EFFMA	Experimental Full-Field Modal Analysis	$\boldsymbol{X}(x,y,\omega)$	Displacement map
EMA	Experimental Modal Analysis	$\boldsymbol{H_d}(x,y,\omega)$	*Receptance* map
ESPI	Electronic Speckle Pattern Interferometry	$\boldsymbol{H_\epsilon}(x,y,\omega)$	Strain FRF map
FEM	Finite Element Model	$\boldsymbol{H_\sigma}(x,y,\omega)$	Stress FRF map
FRF	Frequency Response Function	$\boldsymbol{H_{P\sigma}}(x,y,\omega)$	Principal Stress FRF map
NDT	Non-Destructive Testing	$\boldsymbol{H_{\sigma_{vM}}}(x,y,\omega)$	von Mises Equivalent Stress FRF map
NVH	Noise and Vibration Harshness	$\boldsymbol{\Sigma}(x,y,\omega)$	Dynamic Stress map
ODS	Operative Deflection Shape	$\boldsymbol{\Sigma_P}(x,y,\omega)$	Dynamic Principal Stress map
PSD	Power Spectral Density	$\boldsymbol{\Sigma_{vM}}(x,y,\omega)$	von Mises Equivalent Stress map
SLDV	Scanning Laser Doppler Vibrometer		

the need of any tuning of the numerical synthetic simulator, e.g. FEM. Second: it adds a fine grid of spatially dense displacement sensing dofs, saving the efforts for the best localising of lumped sensors, for the best signal-to-noise ratio and representation of the responses, the sensors' positions being traditionally changed with the loading spectra and awaited structural responses [1]. Third: it does contactless measurements of the structural responses to obtain *receptances* – or displacement over force FRFs – free of any distorting inertia, usually provided instead by lumped sensors (e.g. accelerometers or strain gauges with related cabling). All this is of great advantage for the structural dynamics of lightweight components, especially when the frequency range offers a dense modal base with closely coupled eigenmodes and hard-to-model damping, blending in hardly predictable complex pattern in the ODSs. In this way, the structural *receptances* of the real component are covered in a broad frequency band and highly detailed spatial domain, ready to provide the structural responses on the whole sensed domain with any loading spectrum, which respects the linearity condition under which the *receptances* were estimated.

In the actual deployment of this approach, the fatigue life expectations are described as spatially detailed failure maps in a more macro scale, instead of analyses in lumped locations (e.g. a crack opening point [9]). The fatigue life mapping is here obtained by following the suggestions of [10–12] for random loading, but more specifically [13–17] for the spectral approaches. Many other approaches can be found in literature, as based on strains [18,19], on strain energy [20–22] and on loading-tailored criteria [23–30], but of no specific interest for this introductory work. It can clearly be stated that any other fatigue life predicting approach, rather than what here implemented by [13–17] for the sake of exemplification, can be easily extended from its punctual nature to a fine grid – nearly continuous, with high resolution experiment based full-field *receptances* – detailed mapping.

In such a broad knowledge perspective, for the retained dynamics and for the high resolution mapping achievable, the location of the potential defect plays a relevant role in the crack and failure start. The location of potential defects can be the access to the graded risk map and acceptance criteria, under defined conditions and loading spectra and/or energy injection locations. Any potential defect identified on the mapped domain, whose risk index is below the acceptance threshold, can be retained in the component, under the same service conditions. On the other side, if the risk index is above the acceptance threshold in specific areas of the sample, no defect can be tolerated there, as it can only amplify the life shortening of the component. However, with

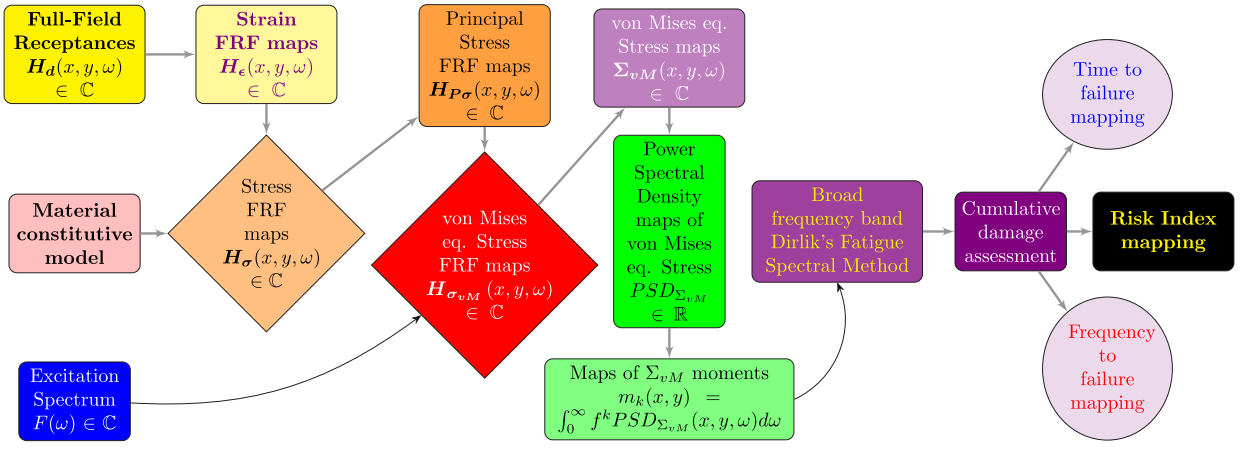

Fig. 1. Overview of the whole process to evaluate the cumulative damage and the *Risk Index* by fatigue spectral methods and presented math in Eqs. (1), (4), (7), (8), (9), (13), (14)–(17), (18), (21)–(22), (23).

different loading spectra or energy injection locations, the risk grading maps can change significantly, as later proved in the paper and conceptually anticipated in [2,5–8], in the early deployment of the concept, but supported by strongly reduced and interpolated ESPI-based *receptances*. This can also mean that a potential defect, located in a specific area of the component, may be accepted only under specific dynamic loading conditions, but not for all the service tasks, turning into a conditional acceptance of the component after proper NDTs in production or maintenance runs, once the nature of the dynamic loading is precisely assessed[1] and known as repeatable.

What follows, briefly detailed in Section 2.1, is devoted to highlight the potentials of this smart approach with extended examples – only reduced into native references, but not interpolated, therefore without potentially added errors from the topology transforms – of *full-field receptances* from high-speed DIC. DIC is another *native* image-based optical non-contact full-field technique, with broader applicability in industrial contexts than ESPI and growing diffusion in testing. ESPI measurements are well known for their enhanced quality datasets, but also for their drawbacks in the acquisition campaign, as better specified below. However, high-speed DIC needs proofs of applicability in dynamic strain & stress evaluations, as well as in fatigue life estimations: this work aims to assess the usability of also DIC-based measurements for risk index mapping, supported by means of the highly accurate derivative approaches that were underlined in [1]. The family of image-based optical non-contact full-field approaches presents no structural dynamics distortions. It also shares the following aspects: a dense grid of sensing locations; a broad frequency band experimental vibration model, with accurate spatial description for complex pattern identification; an experimental dynamic model for strains, obtainable after numerical derivation. The strain mapping from the latter can be used, with material parameters in the constitutive model, to obtain stresses and failure criteria mapping. Accurate maps of cumulative damage distributions for fatigue life assessment can be obtained. Therefore, this shows the advantage of grounding the defect tolerance criteria and risk index maps on image-based full-field measurements, with attention on excitation signature and location.

For the reader that is unfamiliar with optical full-field measurements, a historical perspective might be of help, in order to better appreciate the advantages drawn in this stream of researches. At their earlier steps, optical full-field measurements were mostly qualitative and not competitive in terms of time-to-result [44]. They were therefore mainly used to depict the response shape of a structure at a particular frequency of interest, due to the high spatial sampling offered and high consistency of each measurement degree of freedom with neighbouring locations [45]. Their output was since the beginning a highly detailed spatial domain against the traditional coarse representation obtained by lumped sensor placement. But the increased detail disclosed unprecedented patterns in surface deflection shapes, rapidly changing from frequency to frequency, as function of the complex superposition of the underneath eigensolutions. These non-conventional patterns started to give relevant information on where to better locate the lumped vibration sensors or strain-gauges, the only quantitative instruments at the time.

Since the 1980s an optical *non-native* full-field instrumentation like the SLDV has expanded the technique of contact-less point measurement in time/frequency domains to a fine grid of locations. SLDV was thus extending the concept of the velocity sensors to a spatially detailed acquisition, also without adding inertia to the surface of the specimen under dynamic test. Thus SLDV was till recently considered *the only reference* for the need of spatially detailed FRF measurements in NVH, because SLDV has kept the same peculiarities of previous technologies and proven procedures, just adding more dofs at a reasonable cost.

Among the optical full-field technologies, those based on an imaging sensor – which acquires photons altogether in the whole matrix of light sensible sites (normally in an even denser grid than that of SLDV) – can be called *native*. The *native* technologies approach the measurements from another point of view, that of the acknowledged quality obtainable in the spatial domain, especially in terms of consistency and continuity of the deflection field in the neighbouring dofs, as proved earlier by [45–47]. Among optical *native* full-field technologies, stroboscopic ESPI has given since the years 2000s [48,49] an extremely accurate displacement field at the frequency of interest up to several kHz. But having data at all the lines of a broad frequency band can be prohibitive with ESPI, due to time-consuming stepped sine excitation/acquisition[2], not automated till now. Therefore, ESPI is more suited to laboratory – or controlled environments – measurements, typical of research projects [50–52]. High-speed DIC, with its first commercial prototypes since around 2005, has good detail in the time resolved displacement maps, although the extraction of the correlated fields can still be demanding in terms of calculation time. DIC can be more limited in the frequency domain, as the sensor/electronics bandwidth puts a trade-off between resolution and sampling rate, together with some limitations on the cameras' memory capacity, although nowadays relevant electronics improvements have been made. Furthermore, DIC technology has shown many in-situ applications [53–57], with much greater flexibility also outside controlled set-ups, therefore of wider industrial interest. Therefore, high-speed DIC is the optical *native* full-field technology here adopted for the dynamic testing of the vibrating surface.

The author has been active in full-field measurements to highlight their most advanced applications: some background notes are needed to let the reader appreciate all the progressive development involved in the present work. Since the ESPI-related testing in earlier[3] researches, it became manifest how full-field optical measurements could give relevant and hyper-detailed mapping about the

[1] To be considered also the inquiries by means of frequency based substructuring (FBS) [31–34], transfer path analysis (TPA) [35–40] and multi-input-multi-output (MIMO) vibration testing [41–43].

[2] See also Full field ESPI measurements on a plate: challenging experimental modal analysis, in: Proceedings of the XXV IMAC, Orlando (FL) USA, Feb 19–22, SEM, 2007.

[3] These activities come from the HPMI-CT-1999-00029 *Speckle Interferometry for Industrial Needs* Post-doctoral Marie Curie Industry Host Fellowship project, held in 2004–5 at Dantec Ettemeyer GmbH, Ulm, Germany. See in Proceedings of the IDETC/CIE ASME International Design Engineering Technical Conferences & Computers and Information in Engineering Conference, Long Beach, California, USA, September 24–28, 2005: Dynamic behaviour characterization of a brake disc by means of electronic speckle pattern interferometry measurements, doi:10.1115/DETC2005-84630; Damage location assessment in a composite panel by means of electronic speckle pattern interferometry measurements, doi:10.1115/DETC2005-84631.

local behaviour for enhanced structural dynamics assessments and fatigue spectral methods[4]. These former results were the basis for the fundamental research project TEFFMA[5], a milestone in this track record. TEFFMA project aimed at making a comparison between the state-of-the-art in *native* full-field technologies and the SLDV as reference, to understand if these experimental procedures, in continuous development, can provide NVH applications with enhanced peculiarities. TEFFMA works saw earlier presentations in 2014 [58,59], followed by consolidated reports[6] in 2015. In [50] a gathering of the many activities in TEFFMA was firstly attempted, while in [51] an extensive description of the whole *full-field receptance estimation* was faced and in [60] the EFFMA was detailed together with full-field modeshapes-based model updating attempts. The works in [61] underlined the quality of *native* full-field datasets – especially ESPI and DIC – in broad frequency band dynamic testing. In [1] a precise comparison was made about new achievements for rotational and strain FRF high resolution maps, thanks to the advanced derivative procedures there proposed, but proficiently used here in Section 2.2. But it was in [5] that a risk index was first introduced, as a metric to distinguish failure-exposed areas in a dynamically loaded component, with a focus also on the evidences from damaged fibreglass reinforced composite panels [62]. In the recent paper [6] the variability of ESPI-based risk maps was faced by the changes in the *real-valued* amplitude of the excitation dynamic signature, whereas [7] deals with the effects of different excitation locations and [8] gather both aspects. With [2] the risk index mapping is addressed instead by means of DIC-based full-field *receptances* at the moderate (interpolated) resolution of SLDV in both spatial and frequency domains, while with this work the analysis is made with the original DIC dataset, without any potential distortion coming from the topology transforms and related down-sampling interpolations. To better output the surface zones in danger, where the risk index is above the selected threshold of acceptance, starting from [63] a different colour coding has been introduced, as in evidence in Section 3.3. The recent works on vibro-acoustics [63–66] see the Rayleigh integral approximation – of sound pressure fields radiated by a vibrating surface – fed by the experiment-based full-field *receptances*, showing how the sound pressure mapping can be obtained directly from full-field testing. Furthermore, [63] introduces the identification of the force that is induced by acoustic pressure fields on a structure; the same airborne identified force can be used to assess the fatigue life of a component, while exhibiting the same structural dynamics and responses. Indeed the attention on the high cycles fatigue – from dynamic loading and vibrations – is clearly on the background of this paper: the airborne sound pressure field can be seen as distributed loading, therefore interwoven with NDT & risk grading procedures.

Different works [1,2,5–8,50,51,58–66] were published by the author about the growing *native* optical full-field technologies, their advantages and drawbacks in a broad scenario of applicability and perspectives. It was shown how full-field techniques have started to offer tangible advances for the consistency and continuity of their data fields, with clear repercussions in EFFMA[7] and model updating, vibro-acoustics[8] and derivative calculations (rotational dofs[9], strains, stresses, risk index maps[10]). *Native* technologies can therefore, more and more frequently, cope with the challenges of the most demanding structural testing, without the need of FEM. The sensed *full-field receptance maps* across a broad frequency range can fully characterise the specific structural dynamics of the actual set-up, with all the potential delays of the responses in the superposition of a modally dense dynamics, and with the real damping or boundary conditions, hardly modellable by FEM. They may represent a viable path in order to have the best achievable experiment-based representation of the real behaviour of manufactured and mounted components around their working load levels, also with complex patterns in the dynamic signature of the excitations.

The structure of the article follows Fig. 1. Inside Section 2, a recall of the experiment-based FRF modelling is sketched in Section 2.1, also with a brief description of the testing procedures and attentions about the set-up. Section 2.2 refines the mathematical tools to obtain full-field strain and stress FRF maps, principal stresses and the von Mises equivalent stress maps. All these derivative quantities were refined as *complex-valued* to fully retain – without any approximation – that relevant information in the dynamic behaviour of the real sample, as well as in the dynamic signatures of the excitations. Section 2.3 presents an extended modelling of excitation forces, whose dynamic signature has now all the mathematical characteristics of real-life measured forces, with their typical *complex-valued spectrum*. In particular, the refined *complex-valued* von Mises equivalent stress is used by the spectral methods in Section 2.4, to predict the fatigue life of the components in the extended mapping that full-field techniques can provide. All the results and discussions are gathered in Section 3, where: Section 3.1 highlights how the location of the initial crack can change with the excitation; Section 3.2 introduces the *Risk Index* and the *Threshold of Acceptance* definitions; Section 3.3 pertains the selection of a defect tolerance scheme and its evidences with DIC-based *receptances*; Section 3.4 suggests future researches. Section 4 provides the final conclusions.

[4] See also Fatigue life assessment by means of full field ESPI vibration measurements in: P. Sas (Ed.), Proceedings of the ISMA2008 Conference, September 15–17, Leuven (Belgium); Full field ESPI vibration measurements to predict fatigue behaviour, in: Proceedings of the IMECE2008 ASME International Mechanical Engineering Congress and Exposition, October 31–November 6, Boston (MA), USA.

[5] A. Zanarini, scientific proposer & experienced researcher in the project TEFFMA - Towards Experimental Full Field Modal Analysis, financed by the European Commission - Marie Curie FP7-PEOPLE-IEF-2011 PIEF-GA-2011-298543 grant, 1/02/2013 - 31/07/2015, at the Vienna University of Technology, Austria.

[6] By A. Zanarini, in Proceedings of the ICoEV2015 International Conference on Engineering Vibration, Ljubljana, Slovenia, September 7–10, Univ. Ljubljana & IFToMM, 2015, symposium *Full Field Measurements for Advanced Structural Dynamics*:
Comparative studies on full field FRFs estimation from competing optical instruments, pp. 1559–1568, ID191.
Accurate FRFs estimation of derivative quantities from different full field measuring technologies, pp. 1569–1578, ID192.
Full field experimental modelling in spectral approaches to fatigue predictions, pp. 1579–1588, ID193.
Model updating from full field optical experimental datasets, pp. 773–782, ID196.

[7] See specifically [1,48–51,58–61] for enhanced structural dynamics assessments and model updating.

[8] See specifically [63–66] for vibro-acoustics.

[9] The reader can specifically appreciate in [1,50] the effect of the measurement noise on the estimation of rotational dofs; however, unfortunately due to the complexity or burden of their measurement, the rotational dofs are usually disregarded, whilst they are relevant for the successful build of a reliable dynamic model for complex structures [3,4,33,67–69].

[10] See instead [2,5–8,62] for enhancements of fatigue spectral methods and failure risk grading.

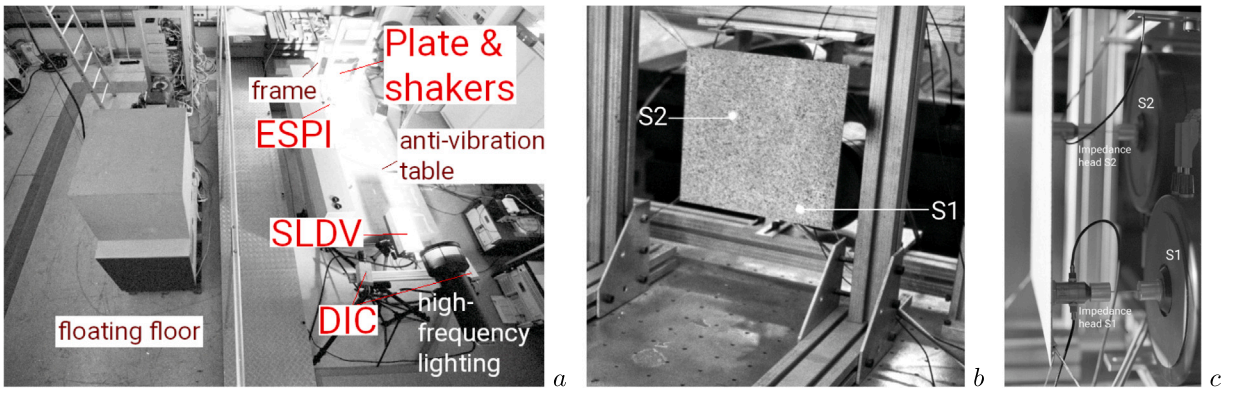

Fig. 2. The lab in the TEFFMA project (see [1,50,51,58–61]): aerial view in *a*, restrained plate sample with highlighted shakers' locations in *b*, 2 shakers on the back of the plate with their impedance heads in *c*.

2. Materials and methods

2.1. Full-field FRFs in TEFFMA project: direct experimental modelling by means of receptances

Here is a brief summary[11] of what was available at TU-Wien as in Fig. 2: a dedicated seismic floor room; a mechanical & electronic workshop with technicians; traditional tools for vibration & modal analysis; but, in particular, there were SLDV, Hi-Speed DIC and stroboscopic ESPI instruments. Accurate studies were needed to understand each technological limit and if a common test for concurrent usage might have been really possible. All this brought to a unique set-up for the comparison of the 3 optical technologies in *full-field FRF estimations*. Great attention was paid to the design of experiments for further research in modal analysis, NVH, vibro-acoustics. After an accurate tuning, a feasible performance overlapping was sought directly out of each instrument, reminding the reader that the same structural dynamics can be sensed in complementary domains, which means frequency for SLDV & ESPI, and time for DIC. The comparisons of the ODSs, directly out of each instrument proprietary software, seemed really promising, but only at a qualitative level, as nothing was precisely super-imposable. Topology transforms were added to have the datasets in the same physical references for appropriate quantitative comparisons.

2.1.1. Brief recall of a direct characterisation by means of full-field receptances

The formulation of *receptance* matrix $\boldsymbol{H_d}(\omega)$, taken from [3,4] as spectral relation between displacements and forces in EMA, will be used for the *full-field FRF estimation*. It describes the dynamic behaviour of a testing system, with potentially multi-input excitation (here 2 distinct shakers), and *many*-output responses (here also several thousands), covering the whole sensed surface, as can be formulated in the following *complex-valued* expression:

$$H_{d_{qf}}(\omega) = \frac{\sum_{m=1}^{N} S^{m}_{X_q F_f}(\omega)}{\sum_{m=1}^{N} S^{m}_{F_f F_f}(\omega)} \in \mathbb{C} \tag{1}$$

where X_q is the output displacement at qth dof induced by the input force F_f at fth dof, while $S^{m}_{X_q F_f}(\omega)$ is the mth cross-power spectral density between input and output, $S^{m}_{F_f F_f}(\omega)$ is the mth auto-power spectral density of the input and ω is the angular frequency, evaluated in N repetitions.

2.1.2. Notes on the sample

The specimen under test was a simple thin rectangular AA7075-T6 plate with external dimensions of 250 × 236 × 1.5 mm. The sample was designed as a lightweight structure to retain a complex structural dynamics within the operative ranges of the used measurement technologies, with its real constraints and damping characteristics. The plate was fixed by wires to a rigid frame on the air-spring optical table (see Figs. 2*a*, *b*) to restrain any excessive rigid-body movement. The plate was in pristine conditions, not to confuse the measurement errors with part's defects. The front-side of the plate was sprayed with a DIC-friendly random noise pattern layer of paint. The excitation was given separately by electrodynamic shakers, in number of 2 for EFFMA in [60]. The shakers, positioned on the back-side of the plate in Fig. 2*c*, were used to fulfil the requirements of the stepped-sine phase-shifting acquisition procedure for ESPI (with an external sine waveform generator), not compatible with impact testing. In SLDV and DIC measurements, instead, LMS Test.Lab system drove the shakers' excitations. Force signals were sampled at the shaker-plate interface by means of the force cells in the impedance heads, to calculate the *receptances* $\boldsymbol{H_d}(x, y, \omega)$ of Eq. (1).

[11] To the interested reader, the most detailed notes of the test campaign appeared in [51], with further suggestions in [1,60,61].

2.1.3. Estimated full-field FRFs & Coherence from optical measurements

Once the experiment-based methodology above was defined as in Eq. (1), *receptance FRF & Coherence function's* maps at specific frequencies and excitation sources were obtained [51,61], to appreciate the spatial consistency and continuity of the data, with clean shapes, sharp nodal lines and excellent *Coherences*, especially from ESPI. The DIC-based datasets here used contain $N_q = 11\,988$ dofs ($N_q = 111 \times 108$, around 2.25 mm structural grid spacing) for 2008 frequency lines, with a frequency space of 0.5 Hz in the 20-1024 Hz frequency range. The datasets were obtained from 2 shakers in different energy injection locations. To be noted that here the DIC-based datasets were only reduced to the common sensed area among the techniques, but not interpolated, therefore adding no noise from the topology transforms.

2.2. Deriving new quantities from full-field receptances

The high quality of the *receptance maps*, also obtainable from DIC, deserves further investigations for novel derivative quantities on the plate surface. In TEFFMA datasets, here used for Section 3, only the *out-of-plane* (z) components of the *receptance map* $\boldsymbol{H_d}(x,y,\omega)$ were above the sensitivity of the measurements; no *in-plane* (x,y) components were above the noise floor, therefore disregarded to null.

2.2.1. Dynamic strain FRFs

The components of the *full-field generalised strain FRFs* $\boldsymbol{H}_{\boldsymbol{\varepsilon}_g}(x,y,\omega) \in \mathbb{C}$ can be obtained, in each map location and frequency line, by means of a robust differential operator[12], applied on the 3D *receptance map* $\boldsymbol{H_d}(x,y,\omega) \in \mathbb{C}$ along $i = (x,y,z)$ and $j = (x,y,z)$ directions:

$$H_\varepsilon(x,y,\omega)_{ij_g} = \frac{1}{2}\left(\frac{\partial \boldsymbol{H_d}(x,y,\omega)_i}{\partial q_j} + \frac{\partial \boldsymbol{H_d}(x,y,\omega)_j}{\partial q_i}\right) \in \mathbb{C}. \tag{2}$$

Being in TEFFMA testing $\boldsymbol{H_d}(x,y,\omega)_x = \boldsymbol{H_d}(x,y,\omega)_y = \boldsymbol{0}$ and $\boldsymbol{H_d}(x,y,\omega)_z$ constant in z, it can be seen that $H_\varepsilon(x,y,\omega)_{xx_g} = H_\varepsilon(x,y,\omega)_{yy_g} = H_\varepsilon(x,y,\omega)_{xy_g} = H_\varepsilon(x,y,\omega)_{yx_g} = H_\varepsilon(x,y,\omega)_{zz_g} = 0$, and only $H_\varepsilon(x,y,\omega)_{xz_g} = H_\varepsilon(x,y,\omega)_{zx_g}$ and $H_\varepsilon(x,y,\omega)_{yz_g} = H_\varepsilon(x,y,\omega)_{zy_g}$ can be populated.

The non-null *bending-related strain FRF tensor* $\boldsymbol{H}_{\boldsymbol{\varepsilon}_b}(x,y,\omega) \in \mathbb{C}$ components, due to *out-of-plane* (z) bending-related displacements/force of the plate of thickness s (here $s = 1.5$ mm), are evaluated as:

$$\begin{aligned} &H_\varepsilon(x,y,\omega)_{xx_b} = -\frac{s}{2}\frac{\partial^2 \boldsymbol{H_d}(x,y,\omega)_z}{\partial x^2} \in \mathbb{C},\ H_\varepsilon(x,y,\omega)_{yy_b} = -\frac{s}{2}\frac{\partial^2 \boldsymbol{H_d}(x,y,\omega)_z}{\partial y^2} \in \mathbb{C}, \\ &H_\gamma(x,y,\omega)_{xy_b} = H_\gamma(x,y,\omega)_{yx_b} = -s\frac{\partial^2 \boldsymbol{H_d}(x,y,\omega)_z}{\partial x \partial y} \in \mathbb{C}. \end{aligned} \tag{3}$$

On the surface, the *total strain FRF tensor* $\boldsymbol{H_\varepsilon}(x,y,\omega) \in \mathbb{C}$ comes from the sum of the previous components:

$$\boldsymbol{H_\varepsilon}(x,y,\omega) = \boldsymbol{H}_{\boldsymbol{\varepsilon}_g}(x,y,\omega) + \boldsymbol{H}_{\boldsymbol{\varepsilon}_b}(x,y,\omega) \in \mathbb{C}, \tag{4}$$

remembering that in this application, with only *out-of-plane* measurable displacements, Eq. (2) can give a limited contribution compared to Eq. (3), also due to the different order of derivatives. With the TEFFMA *out-of-plane* measurements, a specific version of the *total strain FRF tensor*, as $\hat{\boldsymbol{H}}_{\boldsymbol{\varepsilon}}(x,y,\omega)$, can be detailed in the following matrix, with a marked *in-plane* (x,y) prevalence in the magnitudes:

$$\hat{\boldsymbol{H}}_{\boldsymbol{\varepsilon}}(x,y,\omega) = \begin{bmatrix} H_\varepsilon(x,y,\omega)_{xx_b} & H_\gamma(x,y,\omega)_{xy_b} & H_\varepsilon(x,y,\omega)_{xz_g} \\ H_\gamma(x,y,\omega)_{yx_b} & H_\varepsilon(x,y,\omega)_{yy_b} & H_\varepsilon(x,y,\omega)_{yz_g} \\ H_\varepsilon(x,y,\omega)_{zx_g} & H_\varepsilon(x,y,\omega)_{zy_g} & 0 \end{bmatrix} \in \mathbb{C}. \tag{5}$$

Also the *Principal Strain FRF maps* $\boldsymbol{H}_{\boldsymbol{P\varepsilon}}(x,y,\omega)$[13] $\in \mathbb{C}$, from both shakers, can be obtained at each frequency line of the domain by means of a diagonalisation of $\boldsymbol{H_\varepsilon}(x,y,\omega)$, with a *complex-valued* data representation, to retain any phase relation:

$$\boldsymbol{H}_{\boldsymbol{P\varepsilon}}(x,y,\omega) = \boldsymbol{\Phi}_{\boldsymbol{\varepsilon}}^{-1}(x,y,\omega)\boldsymbol{H_\varepsilon}(x,y,\omega)\boldsymbol{\Phi_\varepsilon}(x,y,\omega) = diag[\boldsymbol{H}_{P_1\varepsilon}, \boldsymbol{H}_{P_2\varepsilon}, \boldsymbol{H}_{P_3\varepsilon}](x,y,\omega) \in \mathbb{C}. \tag{6}$$

$\boldsymbol{\Phi_\varepsilon}(x,y,\omega) \in \mathbb{C}$ are the right [70,72–74] *Principal Strain FRF eigenvector* maps. This becomes an impressively adherent characterisation of the experiment-based strain distribution over the sensed surface in spatial and frequency domains.

[12] See [50,58,70,71], but in particular [1] in its Appendix.

[13] $\boldsymbol{H}_{P_1\varepsilon}(x,y,\omega)$ are the *First-*, $\boldsymbol{H}_{P_2\varepsilon}(x,y,\omega)$ are the *Second-*, and $\boldsymbol{H}_{P_3\varepsilon}(x,y,\omega)$ are the *Third-Principal Strain FRF eigenvalue* maps. In this testing, $\boldsymbol{H}_{P_3\varepsilon}(x,y,\omega)$ was orders of magnitude below $\boldsymbol{H}_{P_1\varepsilon}(x,y,\omega)$ and $\boldsymbol{H}_{P_2\varepsilon}(x,y,\omega)$, instead comparable.

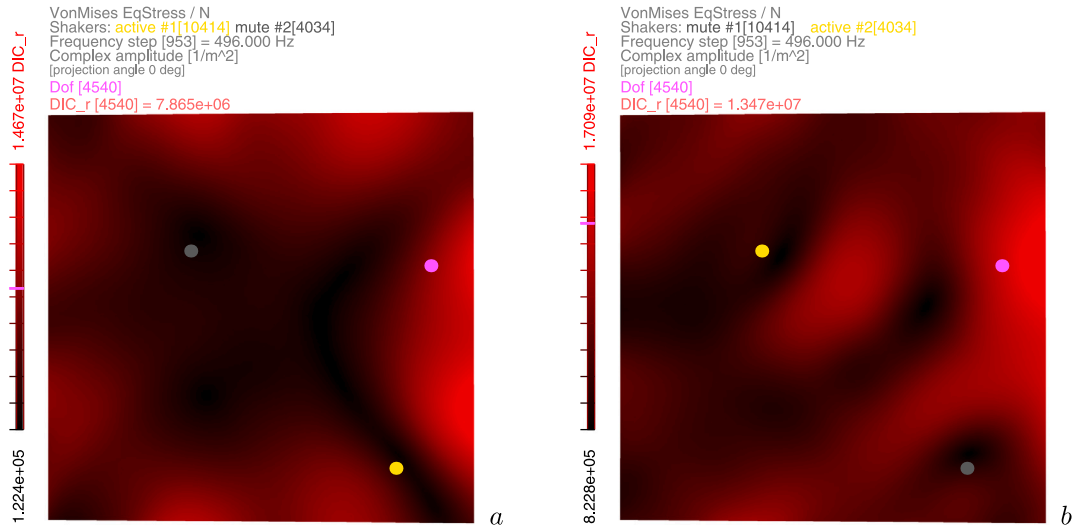

Fig. 3. Examples of *von Mises equivalent stress FRF maps* from optical techniques, direct experimental impedance models in Eq. (9) at 496 Hz, DIC-based examples: from shaker 1 in *a*, from shaker 2 in *b*.

2.2.2. Dynamic stress FRFs

With the introduction of a linear isotropic constitutive model (with the following material parameters: E elastic modulus, ν Poisson ratio, G shear modulus, Λ Lamé constant, here of the aluminium sample in Fig. 2*b*: $E = 71.7$ GPa, $\nu = 0.33$ for the 7075-T6 aluminium alloy), the *Stress FRF tensor* $\boldsymbol{H}_{\boldsymbol{\sigma}}(x,y,\omega) \in \mathbb{C}$ components (expressed in $[1/\mathrm{m}^2]$) can be evaluated from the *total Strain FRFs*:

$$\begin{aligned} &H_{\sigma}(x,y,\omega)_{ii} = 2GH_{\varepsilon}(x,y,\omega)_{ii} + \Lambda\left(H_{\varepsilon}(x,y,\omega)_{xx} + H_{\varepsilon}(x,y,\omega)_{yy}\right) \in \mathbb{C};\\ &H_{\sigma}(x,y,\omega)_{ij} = 2GH_{\varepsilon}(x,y,\omega)_{ij} \in \mathbb{C}; \qquad G = E/2(1+\nu) \in \mathbb{R}; \qquad \Lambda = E\nu/((1+\nu)(1-2\nu)) \in \mathbb{R}. \end{aligned} \tag{7}$$

Therefore, with the constitutive model of any specific material (anisotropic and locally linearised included), the *experiment-based Principal Stress FRF maps* $\boldsymbol{H}_{\boldsymbol{P\sigma}}(x,y,\omega)$[14] $\in \mathbb{C}$ can also be evaluated from the *full-field receptances* $\boldsymbol{H}_{\boldsymbol{d}}(x,y,\omega)$, by means of a diagonalisation of the *Stress FRF tensor* $\boldsymbol{H}_{\boldsymbol{\sigma}}(x,y,\omega)$:

$$\boldsymbol{H}_{\boldsymbol{P\sigma}}(x,y,\omega) = \boldsymbol{\Phi}_{\boldsymbol{\sigma}}^{-1}(x,y,\omega)\boldsymbol{H}_{\boldsymbol{\sigma}}(x,y,\omega)\boldsymbol{\Phi}_{\boldsymbol{\sigma}}(x,y,\omega) = diag[\boldsymbol{H}_{P_1\sigma}, \boldsymbol{H}_{P_2\sigma}, \boldsymbol{H}_{P_3\sigma}](x,y,\omega) \in \mathbb{C}. \tag{8}$$

$\boldsymbol{\Phi}_{\boldsymbol{\sigma}}(x,y,\omega) \in \mathbb{C}$ are the right [70,72–74] *Principal Stress FRF eigenvector* maps. The *Principal Stress FRF maps* $\boldsymbol{H}_{\boldsymbol{P\sigma}}(x,y,\omega)$ can be rearranged in the *von Mises Equivalent Stress FRF* $\boldsymbol{H}_{\boldsymbol{\sigma_{vM}}}(x,y,\omega) \in \mathbb{C}$ general multi-axes stress FRF definition (see [75–77] for further details), independent of the forcing, but only related to the *full-field receptances* $\boldsymbol{H}_{\boldsymbol{d}}(x,y,\omega)$ and the constitutive model:

$$\boldsymbol{H}_{\boldsymbol{\sigma_{vM}}}(x,y,\omega) = \sqrt{\frac{\left[\boldsymbol{H}_{P_1\sigma}(x,y,\omega) - \boldsymbol{H}_{P_2\sigma}(x,y,\omega)\right]^2 + \left[\boldsymbol{H}_{P_2\sigma}(x,y,\omega) - \boldsymbol{H}_{P_3\sigma}(x,y,\omega)\right]^2 + \left[\boldsymbol{H}_{P_1\sigma}(x,y,\omega) - \boldsymbol{H}_{P_3\sigma}(x,y,\omega)\right]^2}{2}}. \tag{9}$$

See Figs. 3*a*, *b* for deployment examples of the *von Mises Equivalent Stress FRF* $\boldsymbol{H}_{\boldsymbol{\sigma_{vM}}}(x,y,\omega)$ in Eq. (9) on the whole spatial mapping of the complex amplitude (expressed in $[1/m^2]$), from both shakers, at the frequency step 953, meaning 496.0 Hz. As in all the *complex-valued* maps proposed, the same projecting angle is kept among the tiles for proper phasing comparisons. Beside each component, the range scale in red tones allows to locate, by means of a magenta line, the level – numerically shown also in the text – reached by the specific function in the structural dof of inquiry, highlighted by the magenta dot (and text). Darker tones correspond linearly to the minimal values in the range, while full brightness pertains to the maximal values. Instead, the yellow dot (and label) on the maps locates the active shaker, while the grey dot (and label) references the mute shaker; here shaker 1 is in structural dof 10 414, shaker 2 in structural dof 4034, as reported in the text of all the figures. Due to the complexity of 3D surfaces and related back-face culling in OpenGL, in some figures the 3 coloured dots might not be visible altogether, or partially hidden. Note the location of the highlighted magenta dof 4540 on the maps in Fig. 3, which is used to extract the single graphs of the corresponding *von Mises Equivalent Stress FRF* $H_{\sigma_{vM}\,4540}(\omega)$ in the whole frequency domain, once obtained from both shakers, as in Figs. 4*a*, *b*. In the latter, the complex phase clearly denotes a restraint in the range $[-\pi, -\pi/2]$, due to the specific formulation of Eq. (9). On the top of the 2D graphs, in the centre, the title of the depicted main function is written in magenta, like the dof

[14] $\boldsymbol{H}_{P_1\sigma}(x,y,\omega)$ are the *First-*, $\boldsymbol{H}_{P_2\sigma}(x,y,\omega)$ are the *Second-*, and $\boldsymbol{H}_{P_3\sigma}(x,y,\omega)$ are the *Third-Principal Stress FRF eigenvalue* maps. In this plane application, $\boldsymbol{H}_{P_3\sigma}(x,y,\omega)$ was very small compared to the others.

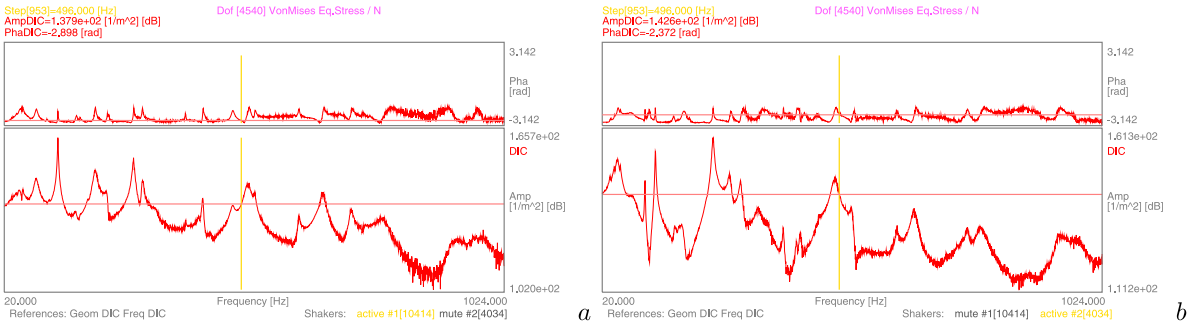

Fig. 4. Examples of *von Mises equivalent stress FRF graphs* from DIC optical technique, direct experimental impedance models from Eq. (9) in the 20-1024 Hz range: from shaker 1 in *a*, from shaker 2 in *b*.

on the maps. On the top left, the frequency line of interest is highlighted in yellow, as well as the corresponding vertical line on the graphs, like a frequency cursor. Just below, the involved functions/parts (in red) are reported with the values at the specific frequency, together with a corresponding horizontal red line in the graphs. In all the 2D graphs, the extremes of the main function (red curve) are annotated in grey text on the right side, as well as the description of the quantity. Where a second function (in black) – with a different scale – is introduced, its extremes and description are written in black text on the right; its full description and punctual value at the specific frequency is reported in the third row on the top, in black, but without any horizontal black line. At the bottom of the graphs, below the line for the extremes of the frequency range, the geometry and frequency references of the dataset are reported in grey text on the left side, whereas the active (yellow) and mute (dark grey) shakers are indicated on the right side.

2.2.3. Dynamic stresses

Once the *complex-valued Stress FRF tensor* $\boldsymbol{H}_{\boldsymbol{\sigma}}(x,y,\omega)$ components are evaluated as in Eq. (7), the *complex-valued* dynamic *Stresses* $\boldsymbol{\Sigma}(x,y,\omega)$ (expressed in [N/m^2]) can be easily evaluated in:

$$\boldsymbol{\Sigma}(x,y,\omega) = \boldsymbol{H}_{\boldsymbol{\sigma}}(x,y,\omega)F(\omega) \in \mathbb{C}, \tag{10}$$

where a generalised scaling *complex-valued* force $F(\omega)$ needs to be defined, as in the following Section 2.3, or obtained from experiments, under the linearity assumption for structural behaviour at the base of Eq. (1).

The dynamic *Principal Stresses* $\boldsymbol{\Sigma}_P(x,y,\omega)$[15] $\in \mathbb{C}$ can also be evaluated in each location of the maps by means of the diagonalisation of the dynamic *Stresses* $\boldsymbol{\Sigma}(x,y,\omega) \in \mathbb{C}$ in Eq. (10), or directly by using the *Principal Stress FRF maps* $\boldsymbol{H}_{\boldsymbol{P\sigma}}(x,y,\omega)$ in:

$$\begin{aligned}\boldsymbol{\Sigma}_P(x,y,\omega) &= \boldsymbol{\Phi}_{\boldsymbol{\sigma}}^{-1}(x,y,\omega)\boldsymbol{H}_{\boldsymbol{\sigma}}(x,y,\omega)\boldsymbol{\Phi}_{\boldsymbol{\sigma}}(x,y,\omega)F(\omega) = \boldsymbol{H}_{\boldsymbol{P\sigma}}(x,y,\omega)F(\omega)\\ &= diag[\boldsymbol{H}_{P_1\sigma}, \boldsymbol{H}_{P_2\sigma}, \boldsymbol{H}_{P_3\sigma}](x,y,\omega)F(\omega) = diag[\boldsymbol{\Sigma}_{P_1}, \boldsymbol{\Sigma}_{P_2}, \boldsymbol{\Sigma}_{P_3}](x,y,\omega) \in \mathbb{C}.\end{aligned} \tag{11}$$

Eventually, and generally (see [75–77] for further details), the *Principal Stresses* $\boldsymbol{\Sigma}_P(x,y,\omega)$ can be used in the *von Mises Equivalent Stress* $\boldsymbol{\Sigma}_{\boldsymbol{vM}}(x,y,\omega) \in \mathbb{C}$ general multi-axes stress definition:

$$\boldsymbol{\Sigma}_{\boldsymbol{vM}}(x,y,\omega) = \sqrt{\frac{\left[\boldsymbol{\Sigma}_{P_1}(x,y,\omega) - \boldsymbol{\Sigma}_{P_2}(x,y,\omega)\right]^2 + \left[\boldsymbol{\Sigma}_{P_2}(x,y,\omega) - \boldsymbol{\Sigma}_{P_3}(x,y,\omega)\right]^2 + \left[\boldsymbol{\Sigma}_{P_1}(x,y,\omega) - \boldsymbol{\Sigma}_{P_3}(x,y,\omega)\right]^2}{2}}. \tag{12}$$

Note that the *von Mises Equivalent Stress* $\boldsymbol{\Sigma}_{\boldsymbol{vM}}(x,y,\omega)$ general multi-axes stress definition easily follows also from Eq. (9), the diagonalisation base $\boldsymbol{\Phi}_{\boldsymbol{\sigma}}(x,y,\omega)$ being the same as in Eq. (11), exploiting the strength of the FRF-based approach – as sketched in the left side of Fig. 1 – here preferred, which evaluates $\boldsymbol{H}_{\boldsymbol{\sigma}_{\boldsymbol{vM}}}(x,y,\omega)$ only once, being excitation independent:

$$\boldsymbol{\Sigma}_{\boldsymbol{vM}}(x,y,\omega) = \boldsymbol{H}_{\boldsymbol{\sigma}_{\boldsymbol{vM}}}(x,y,\omega)F(\omega) \in \mathbb{C}. \tag{13}$$

Both Eqs. (12), (13) give the same result, but Eq. (12) requires the actualisation of $\boldsymbol{\Sigma}_P(x,y,\omega)$ in Eq. (11) at every change of the excitation $F(\omega)$, then its re-evaluation with more operations. Therefore the use of Eq. (12) is discouraged with multiple $F(\omega)$ realisations, or whenever force/input shaping optimisation targets are sought.

The general approach from von Mises [75] is quite basic – albeit widely adopted for its simplicity – with its widely known limits and shortcomings in some specific domains [76,78–80]. It remains partially limited also in the *complex-valued extension* here addressed, as the formulation in Eqs. (12)–(13) does not take fully advantage of the *phase* information, due to the power raising of $()^2$ and $()^{1/2}$ in Eq. (9) or Eq. (12). Again, this is clearly manifest in the phase graphs in Figs. 4*a*, *b*, restrained in the range $[-\pi, -\pi/2]$, and might be a target for further research, when dealing with *complex-valued* datasets for a better representation of the actual structural dynamics.

[15] $\boldsymbol{\Sigma}_{P_1}(x,y,\omega)$ are the *First-*, $\boldsymbol{\Sigma}_{P_2}(x,y,\omega)$ are the *Second-*, and $\boldsymbol{\Sigma}_{P_3}(x,y,\omega)$ are the *Third-Principal Stress eigenvalue* maps. In this plane application, $\boldsymbol{\Sigma}_{P_3}(x,y,\omega)$ was very small compared to the others.

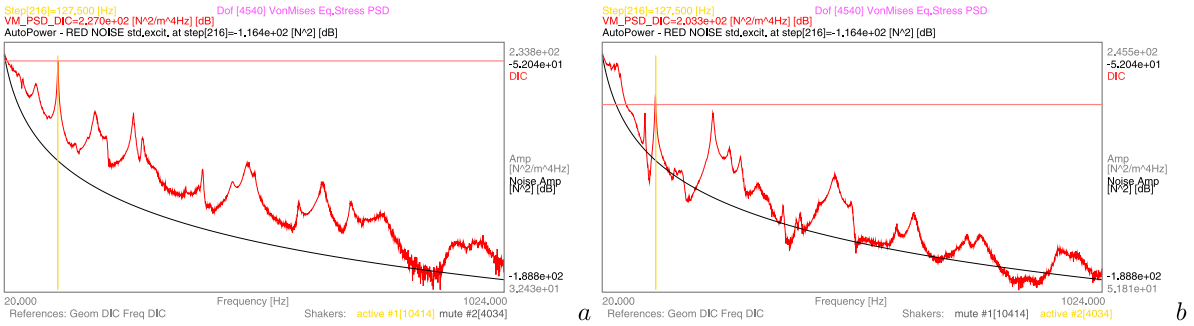

Fig. 5. Examples of *von Mises equivalent stress PSD* log-amplitude graphs (title and traces in red, labels in grey) from DIC optical technique, direct experimental impedance model in dof 4540 from Eq. (18) in the 20-1024 Hz range, superimposed to the Auto Power spectrum of *red noise-std* excitation (all in black) in Eq. (14): from shaker 1 in *a*, from shaker 2 in *b*.

2.3. Formulation of dynamic signatures in excitation forces

In order to appreciate the contribution of experiment-based full-field *receptances*, thanks to their *complex-valued* representation of the real-life structural dynamics, different excitation signatures for $F(\omega) \in \mathbb{C}$ components are discussed in the following subsections. The general shape of the forces is that of the coloured noises, with $\alpha \in [-2, 2]$ defining the *noise colour* ($\alpha = -2$ for *violet noise*, $\alpha = -1$ for *blue noise*, $\alpha = 0$ for *white noise*, $\alpha = 1$ for *pink noise* and $\alpha = 2$ for *red noise*). For all types of excitations, the shared quantities can be defined: $F_0 \in \mathbb{R}$ as the reference amplitude; S_0 as the sinusoidal phase range multiplier; N_p as the number of half cycles of the phase in the range; ω_0 as the starting frequency; $\Delta\omega$ as the frequency range; θ_0 as a reference phase; $\theta(\omega) = S_0 sin(\pi N_p(\omega - \omega_0)/\Delta\omega + \theta_0)$ as a selected phase function; $\beta_{F_0} \in \mathbb{R}$, being $0 \leq \beta_{F_0} \leq 1$, as the level of randomness in the amplitude; $Rand_{F_0}$, or $Rand_\theta$, as a function returning a pseudo-random number in the range 0 to 1; β_θ as the level of randomness in the phase. For all the examples here provided, the following inputs were taken: $F_0 = 0.050$ N, $S_0 = 3.14$ rad, $N_p = 4$, $\theta_0 = \pi/2$ rad, $\beta_{F_0} = 0.15$, $\beta_\theta = 0.30/\pi$, with the respective quantities explained below.

2.3.1. Real-valued coloured noise

A *real-valued coloured noise* excitation $F(\omega)$ can be defined as:

$$F_r(\omega) = \frac{F_0}{\omega^\alpha} \in \mathbb{R}, F_i(\omega) = 0 \in \mathbb{R}, F(\omega) = \left[F_r(\omega), F_i(\omega)\right] \in \mathbb{C}. \tag{14}$$

This means, therefore, that each frequency line component has the same phase, simply put to zero phase lag and null $F_i(\omega)$ imaginary component. This type of noise receives here the label "std", which stands for standard designation, as can be found in Figs. 5, 9 and 13.

2.3.2. Complex-valued coloured noise

A *complex-valued coloured noise* excitation $F(\omega)$ can be defined as:

$$F(\omega) = \frac{F_0}{\omega^\alpha} e^{i\theta(\omega)} \in \mathbb{C}, \tag{15}$$

with $\theta(\omega)$ to address the varying phase with a specific function. This type of noise receives here the label "sp", which stands for sinusoidal phase designation, as can be found in Figs. 6, 10 and 14.

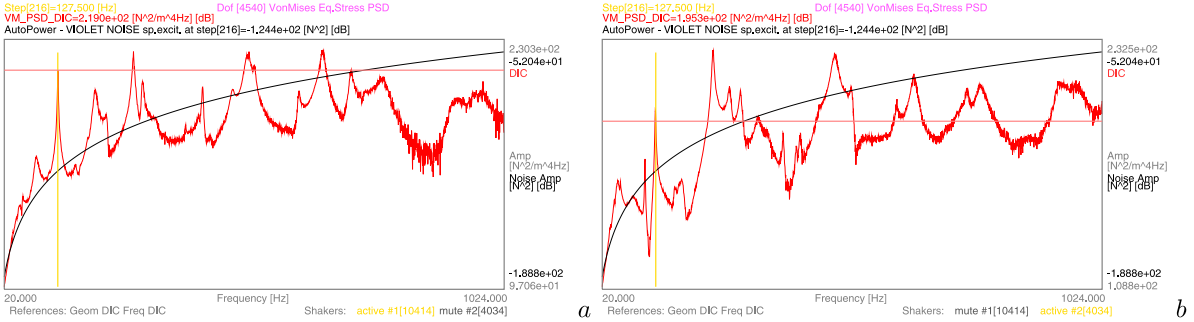

Fig. 6. Examples of *von Mises equivalent stress PSD* log-amplitude graphs (title and traces in red, labels in grey) from DIC optical technique, direct experimental impedance model in dof 4540 from Eq. (18) in the 20-1024 Hz range, superimposed to the Auto Power spectrum of *violet noise-sp* excitation (all in black) in Eq. (15): from shaker 1 in *a*, from shaker 2 in *b*.

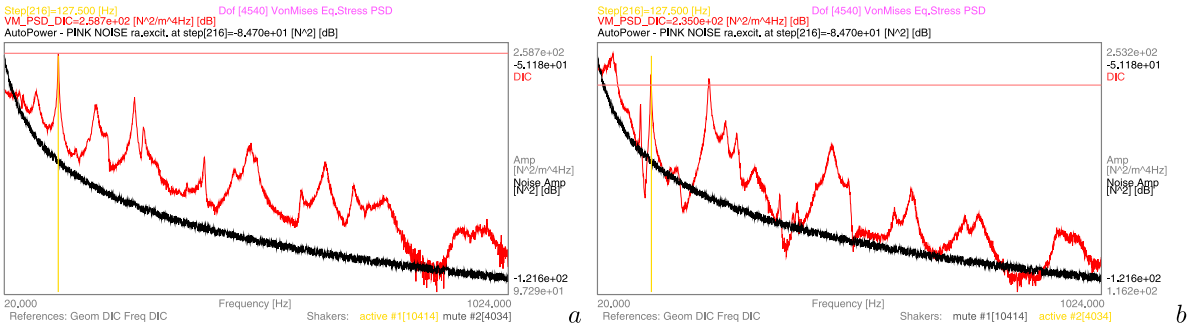

Fig. 7. Examples of *von Mises equivalent stress PSD* log-amplitude graphs (title and traces in red, labels in grey) from DIC optical technique, direct experimental impedance model in dof 4540 from Eq. (18) in the 20-1024 Hz range, superimposed to the Auto Power spectrum of *pink noise-ra* excitation (all in black) in Eq. (16): from shaker 1 in *a*, from shaker 2 in *b*.

2.3.3. Real-valued coloured noise with random amplitude variations

A *real-valued coloured noise* excitation *with random amplitude variations* $F(\omega)$ can be defined as:

$$F_r(\omega) = \frac{F_{0_r}}{\omega^\alpha} \in \mathbb{R},\ F_i(\omega) = 0 \in \mathbb{R},\ F(\omega) = \left[F_r(\omega), F_i(\omega)\right] \in \mathbb{C}. \tag{16}$$

This means therefore that each frequency line component has the same phase, simply put to zero phase lag. Specifically: $F_{0_r} = F_0(1 + \beta_{F_0}(Rand_{F_0} - 0.5))$, where $F_0 \in \mathbb{R}$ can be seen as the reference – or mean – amplitude, around which the randomness occurs. This type of noise receives here the label "ra", which stands for random amplitude – but zero phase lags – designation, as can be found in Figs. 7, 11 and 15.

2.3.4. Complex-valued coloured noise with random amplitude & phase variations

A *complex-valued coloured noise* excitation *with random amplitude & phase variations* $F(\omega)$ can be defined as:

$$F(\omega) = \frac{F_{0_r}}{\omega^\alpha} e^{i\theta_r(\omega)} \in \mathbb{C}. \tag{17}$$

As in Eq. (16), $F_{0_r} = F_0(1 + \beta_{F_0}(Rand_{F_0} - 0.5))$. Identically, $\theta_r(\omega) = \theta(\omega)(1 + \beta_\theta(Rand_\theta - 0.5))$ with $\theta(\omega)$ as the chosen phase function, contaminated by phase random variations. This type of noise receives here the label "rap", which stands for random variations in the amplitude and sinusoidal phase designation, as can be found in Figs. 8, 12 and 16.

It can be clearly seen how this type of signature retraces that of any experiment-based acquisition, with generically varied complex-valued spectrum. Therefore, in these approaches grounded on experiment-based full-field *receptances*, any testing force can be retained with its real-life components, without assumptions nor compromises, except for the respect of the linearity relation between forces and structural responses.

2.4. Cumulative damage & fatigue life assessment by means of spectral methods

With such a broad set of detailed *experiment-based Stress FRF maps* $\boldsymbol{H}_{\boldsymbol{\sigma}}(x, y, \omega)$, excitation independent, we can evaluate cumulative damage with the *spectral methods* for high cycles fatigue in every dof of the sensed surface, with *unprecedented mapping abilities*. A

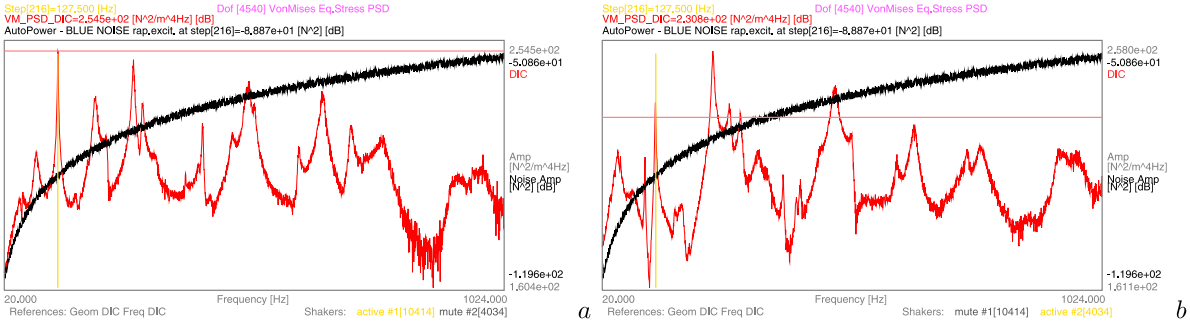

Fig. 8. Examples of *von Mises equivalent stress PSD* log-amplitude graphs (title and traces in red, labels in grey) from DIC optical technique, direct experimental impedance model in dof 4540 from Eq. (18) in the 20-1024 Hz range, superimposed to the Auto Power spectrum of *blue noise-rap* excitation (all in black) in Eq. (17): from shaker 1 in *a*, from shaker 2 in *b*.

spectral method targets the evaluation of an *equivalent range of stress cycles* $S_{eq}(x,y)$, in each location (x,y) of the *experiment-based Stress FRF maps*. $S_{eq}(x,y)$ is representative of the damage inferred by the whole excitation spectrum on the retained dynamics, and can be evaluated in all the locations of the sensed surface. The notation (x,y) is suppressed for compactness in the spatial extension of the specific spectral method parameters below, which must be intended as maps.

Many *spectral methods* (e.g. [13–17,81–91]) are based on $m_k = \int_0^\infty f^k PSD_{\Sigma_{vM}}(\omega)d\omega$, the *kth order moments* of the frequency by $PSD_{\Sigma_{vM}}(\omega)$, the PSD of *von Mises Equivalent Stress*, from which we can obtain other parameters, such as the *effective frequency* $F_{zerocrossing} = F_{zc} = \sqrt{m_2/m_0}$, the *expected number of peaks per unit time* $F_{peaks} = F_p = \sqrt{m_4/m_2}$, and the *irregularity factor* $\gamma = \gamma_2 = F_{zc}/F_p = m_2/\sqrt{m_0 m_4}$.

Recalling what stated in Section 2.2.3 and Eq. (13) about the *complex-valued* nature of the *von Mises Equivalent Stress* $\boldsymbol{\Sigma_{vM}}(x,y,\omega)$, in each location (x,y) of the map the $PSD_{\Sigma_{vM}}(x,y,\omega)$ can be defined as:

$$PSD_{\Sigma_{vM}}(\omega) = PSD_{\Sigma_{vM}}(x,y,\omega) = 2\boldsymbol{\Sigma_{vM}}(x,y,\omega)\boldsymbol{\Sigma^*_{vM}}(x,y,\omega)/\Delta\omega \in \mathbb{R}, \tag{18}$$

where * is the complex conjugate operator and $\Delta\omega$ is the spectral spacing for the granularity in the frequency domain; here the 2 factor comes from the symmetry of the domain, while counting only for the positive frequencies. The *PSD of von Mises Equivalent Stress* is crucial and here evaluated from the *von Mises Equivalent Stress FRFs* $\boldsymbol{H_{\sigma_{vM}}}(x,y,\omega) \in \mathbb{C}$ of Eq. (9), and pivotal in Eq. (13), with the changing coloured noises $F(\omega) \in \mathbb{C}$. $\boldsymbol{H_{\sigma_{vM}}}(x,y,\omega)$ was rendered, and already commented, in the maps at a single frequency in Fig. 3 and in single dof graphs of Fig. 4, from both shakers.

It is important to note that the *experiment-based full-field Stress FRFs* $\boldsymbol{H_\sigma}(x,y,\omega)$ in Eq. (7), with their *principal FRF components* $\boldsymbol{H_{P\sigma}}(x,y,\omega)$ in Eq. (8), or the dynamic *Stresses* $\boldsymbol{\Sigma}(x,y,\omega)$ of Eq. (10) with the related *principal components* $\boldsymbol{\Sigma_P}(x,y,\omega)$ in Eq. (11), are useable with any other spectral method (see e.g. [17]), in particular those that retain the phase relations in the frequency domain, for further comparative works, without the restraining von Mises multi-axes equivalence, as already commented at the end of Section 2.2.3.

2.4.1. Dirlik semi-empirical spectral method parameters

Among the many available ones (see [13–17,81–91]), the *Dirlik semi-empirical spectral method* in [13] was here implemented for the whole (x,y) mapping, as it gives a sound prediction of the fatigue life for wide-frequency-band spectra of stress responses, combining the maps of factors in Eq. (19):

$$\begin{aligned} &\chi_m = \left(m_1/m_0\right)\left(m_2/m_4\right)^{1/2}; \qquad D_1 = 2\left(\chi_m - \gamma^2\right)/\left(1+\gamma^2\right); \qquad R = \left(\gamma - \chi_m - D_1^2\right)/\left(1-\gamma-D_1+D_1^2\right); \\ &D_2 = \left(1-\gamma-D_1+D_1^2\right)/(1-R); \qquad D_3 = 1-D_1-D_2; \qquad Q = 1.25\left(\gamma - D_3 - D_2 R\right)/D_1; \end{aligned} \tag{19}$$

to finally obtain, in each location (x,y), the *Equivalent Range of Stress Cycles* S_{eq} raised to b exponent

$$S_{eq}^b = D_1(2\sqrt{m_0}Q)^b\Gamma(b+1) + (2^{3/2}\sqrt{m_0})^b\Gamma(1+b/2)[D_2R^b + D_3], \tag{20}$$

where $\Gamma()$ is the Gamma function, and the *Time-to-Failure spatial distribution* $T_{failure}$ ([s] or [h]), or its reciprocal *Frequency-to-Failure spatial distribution* $F_{failure}$ ([1/s] or [1/h]), evaluated across all the dofs (x,y) of the maps, function of $S_{eq}(x,y)$, of $F_p(x,y)$ and of the K_r fatigue strength coefficient and b exponent[16], as:

$$T_{failure}(x,y) = K_r/\left[F_p(x,y)S_{eq}^b(x,y)\right], \tag{21}$$

$$F_{failure}(x,y) = \left[F_p(x,y)S_{eq}^b(x,y)\right]/K_r. \tag{22}$$

3. Results and discussion

3.1. Frequency-to-failure with coloured noise excitation

As in [2,5–8,50], new *PSDs* of Eq. (18) are easily obtained from the *stress FRFs* $\boldsymbol{H_\sigma}(x,y,\omega)$ in Eq. (13), by changing the *excitation signature* $F(\omega)$, as modelled in Section 2.3, and *energy injection point* (or shaker). In Figs. 5–8 the $PSD_{\Sigma_{vM}}(\omega)$ are displayed as red curves, whereas the corresponding Auto-Power-spectrum of the excitation is superposed in black. It is manifest how the shape of the complex amplitude of the excitation is able to change the output on the $PSD_{\Sigma_{vM}}(\omega)$: (i) by raising or by lowering specific components in the frequency range of the output; (ii) by transferring the potential randomness of the excitation to the $PSD_{\Sigma_{vM}}(\omega)$. However, the *phase* contributions, with or without randomness, are concealed behind the PSD- and Auto-Power-spectrum- nature of the graphs.

By selecting the *red noise-std real-valued* excitation (Eq. (14), $\alpha = 2$) to multiply the previous $\boldsymbol{H_\sigma}(x,y,\omega)$, the $PSD_{\Sigma_{vM}}(x,y,\omega)$ in Fig. 5 are used in Eq. (22) to evaluate the $F_{failure}$ distribution (in [1/h]), to highlight where the failure should start first, by brighter red tones on higher log-Z axis as in Fig. 9. The $F_{failure}$ maps of Fig. 10 come from the *violet noise-sp complex-valued* excitation, Eq. (15), $\alpha = -2$, which also brought the $PSD_{\Sigma_{vM}}(\omega)$ for the graphs in Fig. 6. A *pink noise-ra real-valued* excitation with randomness

[16] Here K_r = 4.42e+43 Pa^b, b = 4.81 for the 7075-T6 aluminium alloy in [25].

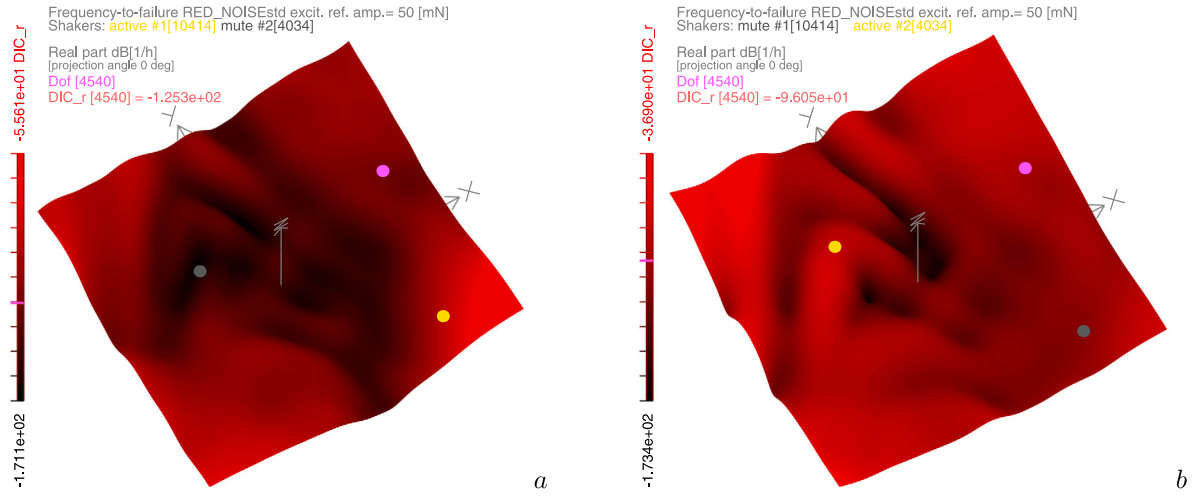

Fig. 9. Examples of *frequency-to-failure distribution* log-amplitude maps of Eq. (22) in [1/h] from *red noise-std excitation* as in Eq. (14), DIC-based examples: from shaker 1 in *a*, from shaker 2 in *b*.

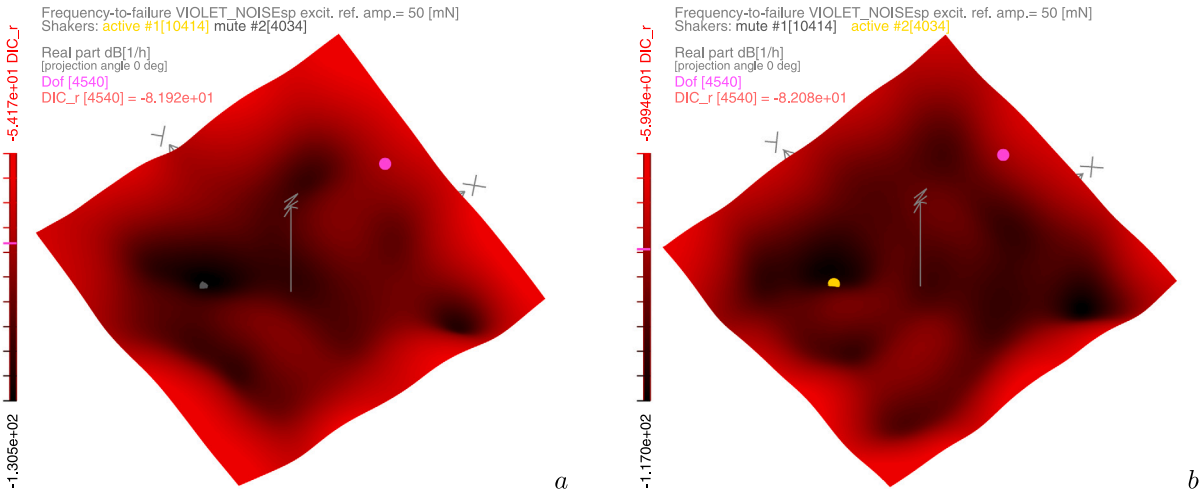

Fig. 10. Examples of *frequency-to-failure distribution* log-amplitude maps of Eq. (22) in [1/h] from *violet noise-sp excitation* as in Eq. (15), DIC-based examples: from shaker 1 in *a*, from shaker 2 in *b*.

in the amplitude, Eq. (16) with $\alpha = 1$, is the source to obtain the $PSD_{\Sigma_{vM}}(\omega)$ for the graphs in Fig. 7 and for $F_{failure}$ maps of Fig. 11. A *blue noise-rap complex-valued* excitation with randomness in the amplitude and phase, Eq. (17) with $\alpha = -1$, is taken to draw the graphs of Fig. 8 and the $F_{failure}$ maps of Fig. 12. To conclude, it was sufficient to change the *dynamic signature* of the $F(\omega)$, and its location, to have different $F_{failure}$ maps, therefore quite different expected life maps of the component under the respective dynamic loading scenario. The dynamic behaviour of the real sample – with real boundary conditions – plays an uttermost role, and no assumptions nor approximations were made to build/tune any synthetic/twin model.

3.2. Definition of the risk index and the defect tolerance criterion

A *defect tolerance criterion* can be built, for usages in manufacturing as well as in exercise, based on the real dynamics, potential location of a defect, and a *Risk Index* definition of ones' choice.

Starting from the predictions of the *experiment-based* $T_{failure}$ maps, an example of ***Risk Index*** *(RI)*[17] can be proposed. The *RI* is based on the *Hours-to-Failure (HtF)* ([h] instead of seconds [s], in Eq. (21)), and can be defined in every dof (x, y) of the map, in a

[17] Any other definition of the risk index is also possible, e.g. by making the level absolute without the relation to the *mean* value [92] in the field, as specific industrial experiences may suggest.

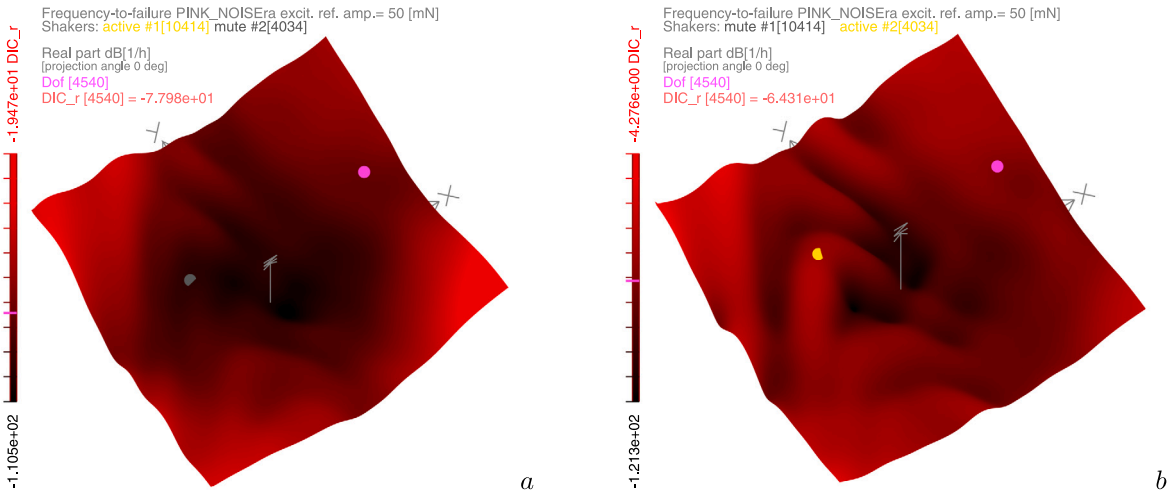

Fig. 11. Examples of *frequency-to-failure distribution* log-amplitude maps of Eq. (22) in [1/h] from *pink noise-ra excitation* as in Eq. (16), DIC-based examples: from shaker 1 in *a*, from shaker 2 in *b*.

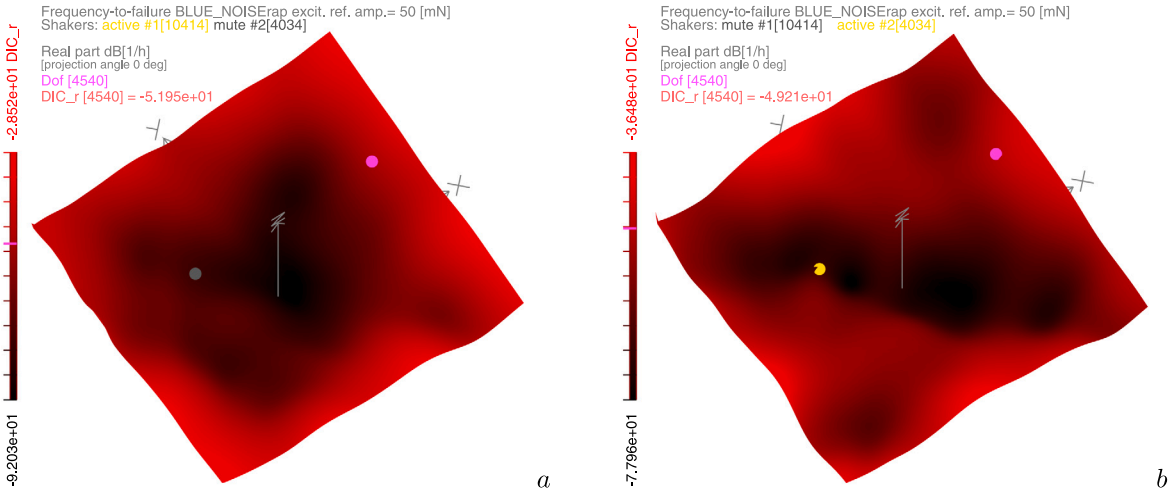

Fig. 12. Examples of *frequency-to-failure distribution* log-amplitude maps of Eq. (22) in [1/h] from *blue noise-rap excitation* as in Eq. (17), DIC-based examples: from shaker 1 in *a*, from shaker 2 in *b*.

decibel shape, relative to the *mean* of the *HtF* distribution:

$$RiskIndex_{[(x,y)]} = RI_{[dof]} = 20log_{10}(\frac{1}{HtF_{[dof]}}) - 20log10(\frac{1}{HtF_{mean}}). \tag{23}$$

A ***Threshold-of-Acceptance*** *(ToA)* can be put to restrain the tolerable value of the defined *Risk Index* for safety reasons. The ToA lies inside the range of the RI values. Once the ToA is defined, a clear grading of the *RI mapping* is achieved on the whole spatial domain, where also defects find their collocation. Therefore the *defect tolerance criterion*, with the related safety assurance, can be said applicable in all the areas where the defined RI is below the ToA: the **defect tolerance** is possible *with safety* if $RI \leq ToA$.

The colour coding of the *RI* maps is inherited from [2], now using red tones for DIC technology, instead of green tones for ESPI. The *RI* maps have been enhanced by using the ToA level as colour discriminant: all the dofs where the $RI \leq ToA$ are displayed in red tones, ramping from zero brightness (black) of the lowest RI in the range, to the brightness level of the ToA, as percentage of ToA over the amplitude of the RI range; all the dofs where the $RI > ToA$ are displayed in grey tones with brightness varying from the level of the ToA over the amplitude of the RI range, till the full brightness (pure white) at the maximal RI value. This clearly makes a distinction of the zones below or above the ToA defined. It becomes trivial to separate safe areas (in red tones) from dangerous ones (in grey tones), therefore assessing where a potential defect may be tolerated and where not. In addition, the RI value of the inquiry dof on the maps – there displayed by a magenta dot – is reported on the RI range bar on the left of the pictures by means of a magenta line.

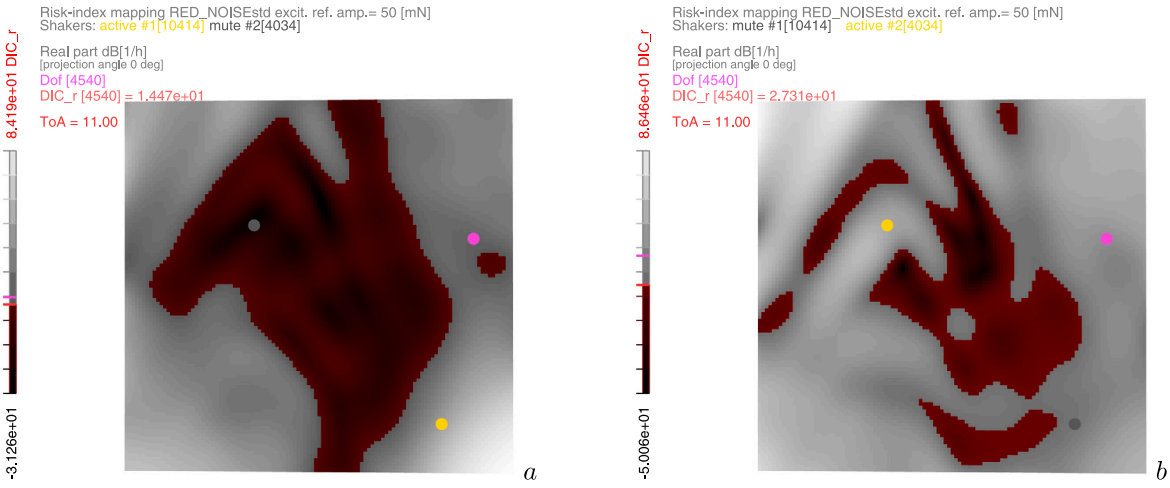

Fig. 13. Examples of *Risk Index mapping* in dof 4540, with *red noise excitation* from shaker 1 in *a* and shaker 2 in *b*. If *ToA = 11*, a defect in dof 4540 is tolerable when the excitation comes from shaker 1, whereas is intolerable, thus dangerous, if shaker 2 gives the excitation.

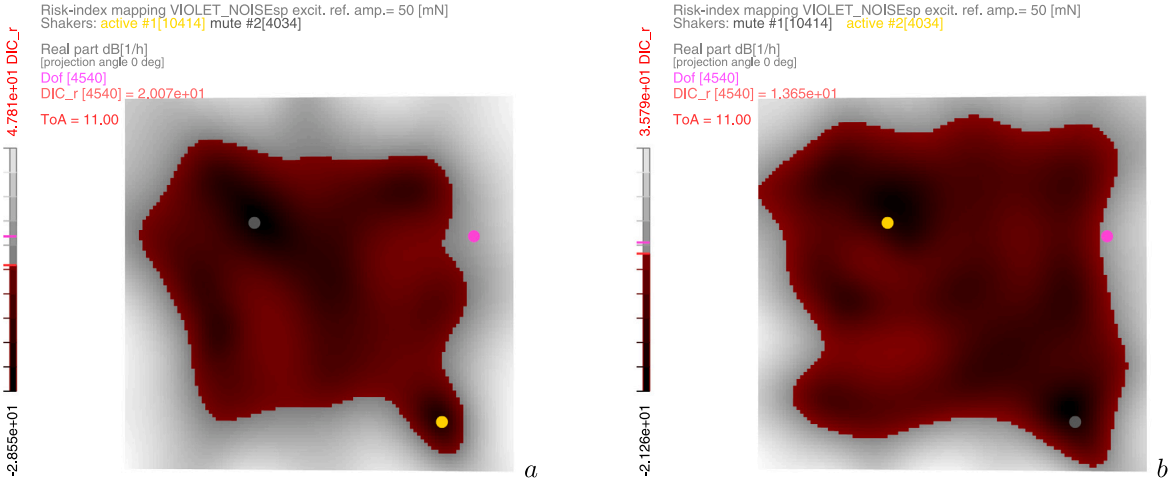

Fig. 14. Examples of *Risk Index mapping* in dof 4540, with *violet noise excitation* from shaker 1 in *a* and shaker 2 in *b*. If *ToA = 11*, a defect in dof 4540 is intolerable, thus dangerous, with both energy injection points.

3.3. Examples of defect tolerance criterion, based on full-field dynamic testing & risk index

As well as was demonstrated with the $\boldsymbol{\Sigma}_{\boldsymbol{vM}}(x, y, \omega)$ graphs of Figs. 5–8 and the $F_{failure}$ maps of Figs. 9–12, the different excitations and energy injection locations bring their respective *RI maps*, for a total of 8 different maps, due to 4 different excitations and 2 locations. In the examples of Fig. 13, evaluated from the *red noise-std real-valued* excitation (Eq. (14), $\alpha = 2$), the location of the magenta dof 4540, with a *ToA* of 11 in Eq. (23), informs if, according to the proposed *RI* and shaker location, the potential defect there located is tolerable or not, with clear safety repercussions in production or exercise. In both locations, $RI_{4540} > 11$, therefore any potential defect in dof 4540 would be in a dangerous – and not allowed – location, thus bringing to the rejection of the component/part under safety trial. However, the reached RI_{4540} level in Fig. 13*a* is of 14.47 [1/h dB] (31.54% above ToA), against the 27.31 [1/h dB] (148.27% above ToA) in Fig. 13*b*. This tells how more dangerous the location in the case of shaker 2 injection is, and also underlines the risk grading ability that is retained in the *RI* along the whole mapping of sampled locations. Also note how different the *RI* maps are when the energy injection location changes.

The *RI* maps of Fig. 14, obtained from the *violet noise-sp complex-valued* excitation (Eq. (15), $\alpha = -2$), might appear, instead, more similar than those in Fig. 13, but the *RI* ranges are quite different. There results that the $RI_{4540} > 11$ with both shakers, but in Fig. 14*a* the RI_{4540} with shaker 1 is equal to 20.07 [1/h dB] (82.45% above ToA), while in Fig. 14*b* with shaker 2 the RI_{4540} reaches 13.65 [1/h dB] (24.09% above ToA), with a clear sign of a lower danger (indeed dof 4540 is closer to the red-toned area).

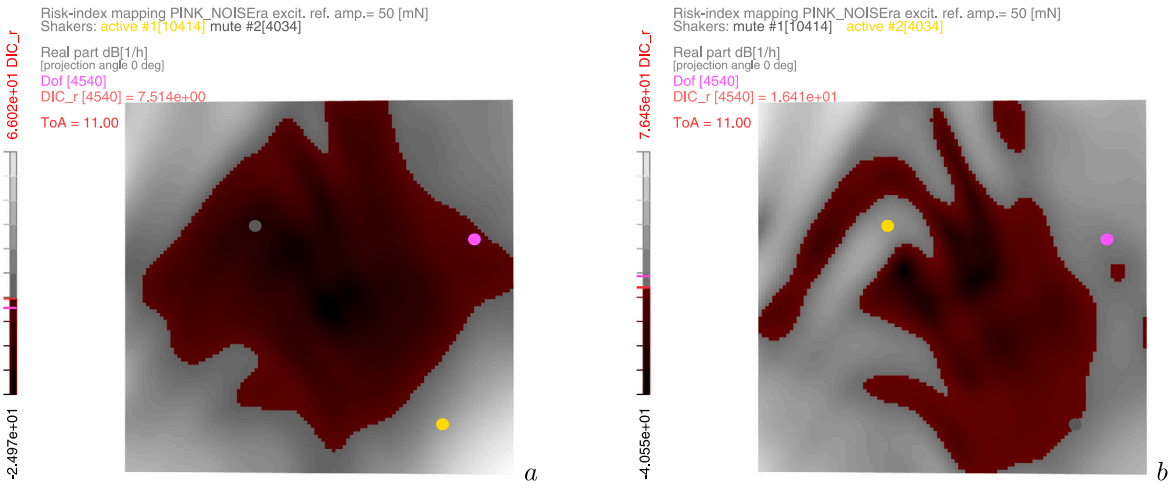

Fig. 15. Examples of *Risk Index mapping* in dof 4540, with *pink noise excitation* from shaker 1 in *a* and shaker 2 in *b*. If $ToA = 11$, a defect in dof 4540 is tolerable when the excitation comes from shaker 1, whereas is intolerable, thus dangerous, if shaker 2 gives the excitation.

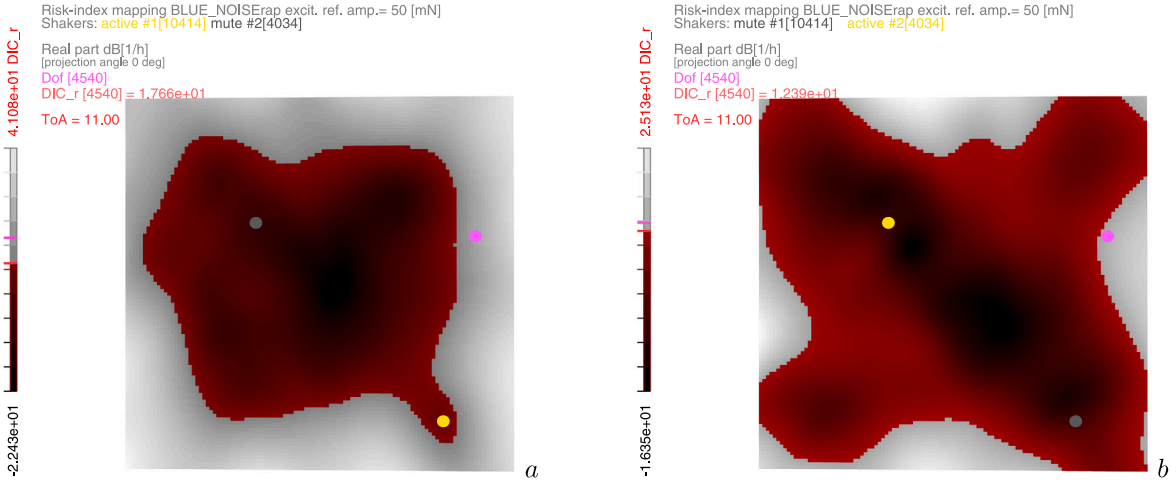

Fig. 16. Examples of *Risk Index mapping* in dof 4540, with *blue noise excitation* from shaker 1 in *a* and shaker 2 in *b*. If $ToA = 11$, a defect in dof 4540 is intolerable, thus dangerous, with both energy injection points.

The examples of Fig. 15, obtained instead with a *pink noise-ra real-valued* excitation with randomness in the amplitude only (Eq. (16), $\alpha = -1$) from both shakers, show again completely different RI maps, due to the changed emphasis on the broad frequency band contributions. But only in Fig. 15*a* is the $RI_{4540} \leq 11$ (7.51 [1/h dB], or 31.72% below ToA, therefore considered as *safe*) among the whole examples here provided. Instead, the same excitation, once it comes from shaker 2, causes $RI_{4540} > 11$ (16.41 [1/h dB], or 49.18% above ToA, now dangerous again.

Finally, the RI maps of Fig. 16, obtained from the *blue noise-rap complex-valued* excitation with randomness in both the complex amplitude and phase (Eq. (17), $\alpha = 1$), appear again, as expectable, quite different in the shape of safe areas and RI ranges. There results that the $RI_{4540} > 11$ with both shakers, but in Fig. 16*a* the RI_{4540} with shaker 1 is equal to 17.66 [1/h dB] (60.54% above ToA), while in Fig. 16*b* with shaker 2 the RI_{4540} reaches 12.39 [1/h dB] (12.63% above ToA), with a clear sign of a less danger (again dof 4540 is relatively close to the red-toned area).

Therefore, a potential defect in dof 4540 might be tolerable – or acceptable – only in the scenario where the excitation has that specific *pink noise-sp real-valued* excitation with randomness in the amplitude, coming from shaker 1. This underlines the effectiveness of *full-field FRF-based Risk Index* mapping: it was sufficient to change the *dynamic signature* of the excitation, and its location, to understand how the problematic (grey) areas on the sample wildly changed, much beyond any instinctive – and unsupported – prediction from a potential blending of analytical eigenmodes from ideal boundary conditions and damping.

The concept can be further expanded by any different *coloured noise excitation* $F(\omega)$ as modelled in Section 2.3, or also by *in-field measured forces*, to evaluate the related $PSD_{\Sigma_{vM}}(\omega)$ as in Eq. (18) and the corresponding RI map in Eq. (23). It was also proved how

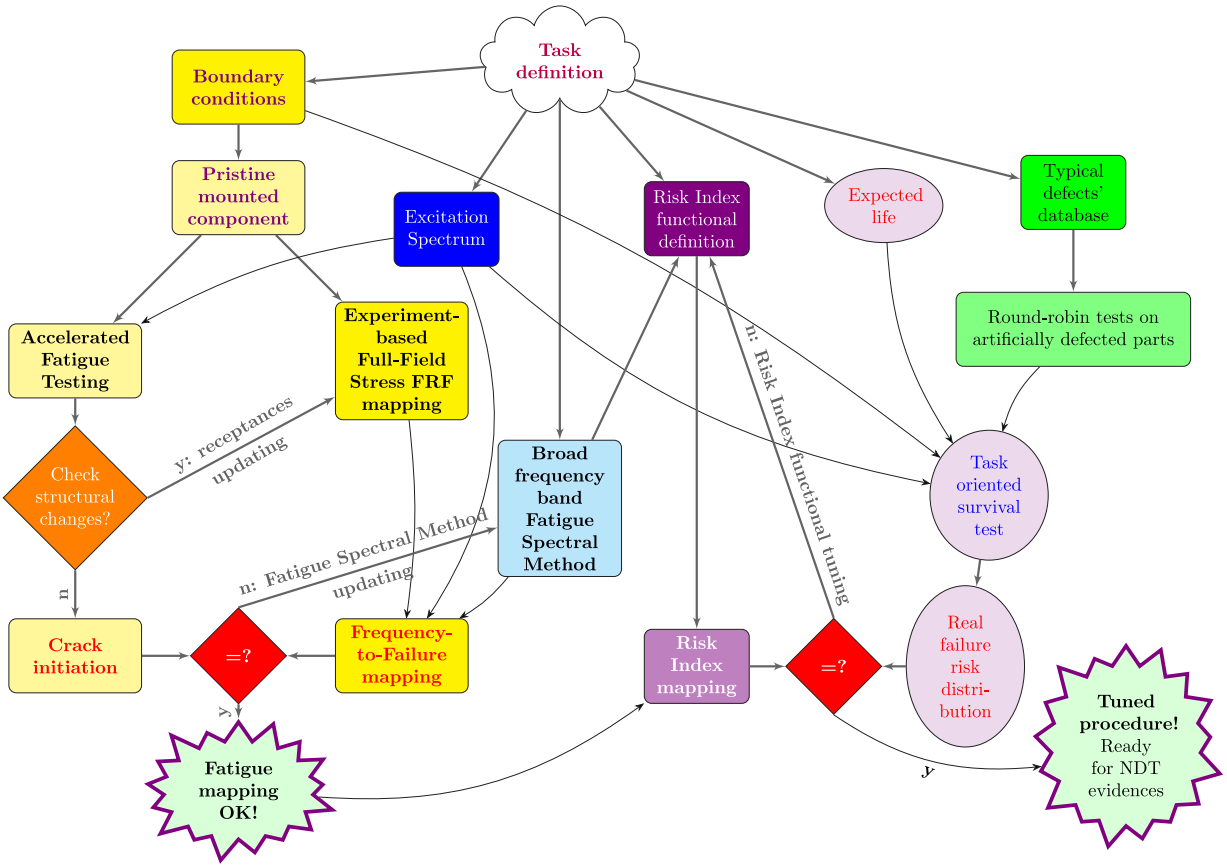

Fig. 17. Overview of the suggested steps in future proofs of the whole approach process to evaluate the cumulative damage and the *Risk Index* by fatigue spectral methods.

DIC can be proficiently employed in these *full-field measurement-based* assessments, once the right testing campaigns are properly conducted around the working conditions of the samples, about which the defects need answers on acceptability or risk grading.

3.4. Future proofs

Future testing and researches are needed for a comprehensive proof, before this whole methodology finds applicability to more complex structural parts, for quality checks in production or for maintenance in service. Three main steps to tune the methodology are suggested and sketched in Fig. 17: (i) tune the selected fatigue spectral method with the testing; (ii) tune the RI function in round-robin tests with artificially defected samples; (iii) check the whole procedure with evidences from full-field NDT. Basic is the task definition, which, beyond the sample type, includes: (a) the boundary conditions and (b) the excitation spectrum (with the potential aid of FBS [31–34], TPA [35–40] and MIMO vibration testing [41–43]); (c) a specific fatigue spectral method – among the many available (see [13–17,81–91]) – for the loading scenario; (d) the RI functional definition; (e) the expected life and (f) the typical defects' database. For the first methodology tuning step (i), the core part to assess is the damage distribution in $T_{failure}$ in Eq. (21), or $F_{failure}$ in Eq. (22), coming from the wanted broad frequency band excitation. Attention should be paid to check how the damage severity can affect the sensed surface of pristine samples till the starting of a fracture [93,94], when the structural dynamics changes considerably. A reasonable number of tests on pristine samples might be needed for stronger statistical evidences [92], with care to the repeatability of manufacturing and boundary conditions. Once a fracture starts, its location needs to be compared to the aforementioned maps and proper tuning of the fatigue modelling is needed, with the selected fatigue spectral method. During these accelerated fatigue tests, periodically and before the crack initiation, new evaluations of the *receptances* are suggested, to assess if the structure is not changing and the linearity assumptions are still valid. In the eventuality changes occur, all the involved evaluations must be updated. For the second methodology tuning step (ii), once the fatigue spectral method finds agreement with the real accelerated testing, a calibration of a selected RI function is suggested. RI calibration might be based on the typical defects that may occur in the specific component and the relation they might have with fatigue evidences and failures. The RI function can be different than what exemplified in Eq. (23), taking care of specific conditions in the formulation and ToA, as suggested by evidences of failure in a broad database (e.g. by inserting peaks or specific values, or other functional relations, as already suggested

in Section 3.2). Task oriented survival tests with artificially defected samples, carrying the meaningful defects in dangerous and safe areas, should be arranged under the same task definitions, to assess the whole defect tolerance procedure and refine the *RI* definition. For the third methodology tuning step (iii), real-life samples, with the defects highlighted by full-field NDT evidences, should be dynamically tested under the same task definitions to finally check the whole approach.

Nevertheless, the *damage location assessment* on real components may play a relevant role within the *defect tolerance strategies*. The chosen Figs. 13–16 above were just examples from virtual excitations, but the same ESPI-based *NDT* shown in [62,95] may give a *real defect distribution map*, which can be the input in *RI maps*, here obtained by DIC full-field dynamic testing (instead of ESPI in [5,6]). In this coupled strategy, the real location of the defect on the map can tell if it can be accepted or not, in quality checks during manufacturing or in maintenance programs in exercise, once the real structural dynamics and excitation signature are fully known without simplifications. Therefore the *NDT*, the *structural dynamics'* measurement and the *defect tolerance criteria* can all be based on *full-field dynamic testing*, to put the most advanced experimental structural dynamics' knowledge into higher safety targets.

4. Conclusions

This extended paper has shown how a methodologically sound *risk tolerance assessment* can be run also from *DIC-based full-field receptances*, which have less restraints in their estimation than those from the ESPI approach. By means of high-resolution and high-quality DIC-based *receptances*, which retain the real dynamic behaviour of the lightweight structure as linearised around the working levels, it was therefore possible to run the accurate evaluation of *Strain FRF maps*, of *Stress-* and *von Mises Equivalent Stress-FRF maps* with a proper constitutive model. The introduction of *complex-valued coloured noise excitations* brought to the evaluation of *von Mises Equivalent Stress-PSDs* and of the *fatigue life predictions* by means of *spectral methods*, directly from *experimental DIC-based full-field FRFs*, without any further simplifying synthetic hardly-tunable model. The defined *Risk Index maps* permitted to grade the dangerous locations of potential defects, with a selected *threshold of acceptance*, with repercussions in manufacturing and exercise.

Experimental optical full-field measurement techniques, also in the DIC variant, are becoming mature and reliable for a *risk tolerance assessment* in production and working conditions, because of their ability to identify defects and to retain a refined and dense structural dynamics in both the frequency and spatial domain, directly from real samples and without any FE model, which always needs careful updating. Furthermore, these experiment-based full-field techniques provide new benchmarks for all the simulations from any synthetic model, for a clear advancement of designing procedures and of virtual prototyping.

CRediT authorship contribution statement

Alessandro Zanarini: Writing – review & editing, Writing – original draft, Visualization, Validation, Supervision, Software, Resources, Project administration, Methodology, Investigation, Funding acquisition, Formal analysis, Data curation, Conceptualization.

Declaration of competing interest

The authors declare that they have no known competing financial interests or personal relationships that could have appeared to influence the work reported in this paper.

Data availability

The data that has been used is confidential.

Acknowledgments

This activity is a spin-off of the TEFFMA (Towards Experimental Full Field Modal Analysis) project, funded by the European Commission at the Technische Universitaet Wien, through the Marie Curie FP7-PEOPLE-IEF-2011 PIEF-GA-2011-298543 grant, for which the Research Executive Agency is greatly acknowledged. TU-Wien, in the person of Professor Wassermann and his staff, are kindly acknowledged for having hosted the TEFFMA project of the author at the *Schwingungs- und Strukturanalyse*/Optical Vibration Measurement Laboratory. The Linux-based workstation, used to extensively process the datasets and code in C-language/OpenMP/OpenGL the whole outputs, was provided by the author out of his own savings. Professor Roberta Mullini is wholeheartedly acknowledged for her care in the English proofreading of the text.

References

[1] A. Zanarini, Chasing the high-resolution mapping of rotational and strain FRFs as receptance processing from different full-field optical measuring technologies, Mech. Syst. Signal Process. 166 (2022) 108428, http://dx.doi.org/10.1016/j.ymssp.2021.108428.

[2] A. Zanarini, Exploiting DIC-based full-field receptances in mapping the defect acceptance for dynamically loaded components, Procedia Struct. Integr. 54C (2024) 99–106, http://dx.doi.org/10.1016/j.prostr.2024.01.061, paper ID 022@ICSI2023 The 5th International Conference on Structural Integrity, 28 August - 1 September, 2023.

[3] W. Heylen, S. Lammens, P. Sas, Modal Analysis Theory and Testing, second ed., Katholieke Universiteit Leuven, Leuven (Belgium), ISBN: 90-73802-61-X, 1998.

[4] D.J. Ewins, Modal Testing - Theory, Practice and Application, second ed., Research Studies Press Ltd., Baldock, Hertfordshire, England, 2000, p. 400, URL https://www.wiley.com/en-it/Modal+Testing%3A+Theory%2C+Practice+and+Application%2C+2nd+Edition-p-9780863802188.

[5] A. Zanarini, On the defect tolerance by fatigue spectral methods based on full-field dynamic testing, Procedia Struct. Integr. 37 (2022) 525–532, http://dx.doi.org/10.1016/j.prostr.2022.01.118, paper ID 105, ICSI 2021 The 4th International Conference on Structural Integrity.
[6] A. Zanarini, Introducing the concept of defect tolerance by fatigue spectral methods based on full-field frequency response function testing and dynamic excitation signature, Int. J. Fatigue 165 (2022) 107184, http://dx.doi.org/10.1016/j.ijfatigue.2022.107184.
[7] A. Zanarini, About the excitation dependency of risk tolerance mapping in dynamically loaded structures, in: ISMA2022 Including USD2022 - International Conference on Noise and Vibration Engineering, Leuven, Belgium, September 12-14, KU Leuven, 2022, pp. 3804–3818, URL https://past.isma-isaac.be/downloads/isma2022/proceedings/Contribution_208_proceeding_3.pdf, paper ID 208 in Vol. Structural Health Monitoring.
[8] A. Zanarini, Risk tolerance mapping in dynamically loaded structures as excitation dependency by means of full-field receptances, in: IMAC XLI - International Modal Analysis Conference - Keeping IMAC Weird: Traditional and Non-Traditional Applications of Structural Dynamics, Austin (Texas), USA, Springer Nature Switzerland AG & SEM Society for Experimental Mechanics, 2023, pp. 43–56, http://dx.doi.org/10.1007/978-3-031-34910-2_9, paper ID 14648 - chapter 9, in J. Baqersad, D. Di Maio (eds.), Computer Vision & Laser Vibrometry, Volume 6, Conference Proceedings of the Society for Experimental Mechanics Series.
[9] B.V. Farahani, F. Direito, P.J. Sousa, P.J. Tavares, V. Infante, P.P. Moreira, Crack tip monitoring by multiscale optical experimental techniques, Int. J. Fatigue 155 (2022) 106610, http://dx.doi.org/10.1016/j.ijfatigue.2021.106610.
[10] A. Buch, Prediction of the comparative fatigue performance for realistic loading distributions, Prog. Aerosp. Sci. 33 (1997) 391–430, http://dx.doi.org/10.1016/S0376-0421(96)00010-3, Elsevier Science Ltd.
[11] A. Fatemi, L. Yang, Cumulative fatigue damage and life prediction theories: a survey of the state of the art for homogeneous materials, Int. J. Fatigue 20 (1998) 9–34, http://dx.doi.org/10.1016/S0142-1123(97)00081-9, Elsevier Science Ltd.
[12] T.J. George, J. Seidt, M.H.H. Shen, T. Nicholas, C.J. Cross, Development of a novel vibration-based fatigue testing methodology, Int. J. Fatigue 26 (2004) 474–486, http://dx.doi.org/10.1016/j.ijfatigue.2003.10.012, Elsevier Science Ltd.
[13] T. Dirlik, Application of Computers in Fatigue Analysis (Ph.D. thesis), University of Warwick, 1985, URL http://wrap.warwick.ac.uk/2949/.
[14] ESDU, Spectral methods for the estimation of fatigue life 06011, in: Estimation of Fatigue Life of Structures Subjected To Random Loading, in: Vibration and Acoustic Fatigue Series, Vol. 9, ESDU International Plc, London, 2006, pp. 1–56, https://www.esdu.com/cgi-bin/ps.pl?t=doc&p=esdu_06011a.
[15] E.N. Dowling, Estimating fatigue life, in: Fatigue and Fracture, in: ASM Handbook, Vol. 19, ASM International Handbook Committee, 1996, pp. 1–23, http://dx.doi.org/10.31399/asm.hb.v19.a0002365.
[16] D. Benasciutti, R. Tovo, Spectral methods for lifetime prediction under wide-band stationary random processes, Int. J. Fatigue 27 (8) (2005) 867–877, http://dx.doi.org/10.1016/j.ijfatigue.2004.10.007, Cumulative Fatigue Damage Conference - University of Seville 2003.
[17] T. Dirlik, D. Benasciutti, Dirlik and Tovo-Benasciutti spectral methods in vibration fatigue: A review with a historical perspective, Metals 11 (9) (2021) http://dx.doi.org/10.3390/met11091333.
[18] D.G. Shang, D.K. Wang, M. Li, W.X. Yao, Local stress-strain field intensity approach to fatigue life prediction under random cyclic loading, Int. J. Fatigue 23 (2001) 903–910, http://dx.doi.org/10.1016/S0142-1123(01)00051-2, Elsevier Science Ltd.
[19] A.K. Lynn, D.L. DuQuesnay, Computer simulation of variable amplitude fatigue crack initiation behaviour using a new strain-based cumulative damage model, Int. J. Fatigue 24 (2003) 977–986, http://dx.doi.org/10.1016/S0142-1123(02)00007-5, Elsevier Science Ltd.
[20] S.K. Koh, Fatigue damage evaluation of a high pressure tube steel using cycle strain energy density, Int. J. Press. Vessels Pip. 79 (2002) 791–798, http://dx.doi.org/10.1016/S0308-0161(02)00135-7, Elsevier Science Ltd.
[21] T. Lagoda, Energy models for fatigue life estimation under uniaxial random loading. Part I: The model elaboration, Int. J. Fatigue 23 (2001) 467–480, http://dx.doi.org/10.1016/S0142-1123(01)00016-0, Elsevier Science Ltd.
[22] T. Lagoda, Energy models for fatigue life estimation under uniaxial random loading. Part II: Verification of the model, Int. J. Fatigue 23 (2001) 481–489, http://dx.doi.org/10.1016/S0142-1123(01)00017-2, Elsevier Science Ltd.
[23] J. Ling, J. Pan, An engineering method for reliability analyses of mechanical structures for long fatigue lives, Reliab. Eng. Syst. Saf. 56 (1997) 135–142, http://dx.doi.org/10.1016/S0951-8320(97)00012-4, Elsevier Science Ltd.
[24] M. Kuroda, Extremely low cycle fatigue life prediction based on a new cumulative fatigue damage model, Int. J. Fatigue 24 (2001) 699–703, http://dx.doi.org/10.1016/S0142-1123(01)00170-0, Elsevier Science Ltd.
[25] ESDU, Fatigue damage and life under random loading 06009, in: Estimation of Fatigue Life of Structures Subjected To Random Loading, in: Vibration and Acoustic Fatigue Series, Vol. 9, ESDU International Plc, London, 2006, pp. 1–41, https://www.esdu.com/cgi-bin/ps.pl?sess=unlicensed_1240524092211wvt&t=doc&p=esdu_06009b.
[26] I. Marines, X. Bin, C. Bathias, An understanding of very high cycle fatigue of metals, Int. J. Fatigue 25 (2003) 1101–1107, http://dx.doi.org/10.1016/S0142-1123(03)00147-6, Elsevier Science Ltd.
[27] F. Sherratt, N. Bishop, T. Dirlik, Predicting fatigue life from frequency domain data, J. Eng. Integr. Soc. (EIS) 18 (2005) 12–16, URL https://www.researchgate.net/publication/284415325_Predicting_fatigue_life_from_frequency_domain_data.
[28] Y.L. Lee, T. Tjhung, A. Jordan, A life prediction model for welded joints under multiaxial variable amplitude loading histories, Int. J. Fatigue 29 (2007) 1162–1173, http://dx.doi.org/10.1016/j.ijfatigue.2006.09.014, Elsevier Science Ltd.
[29] P. Wolfsteiner, S. Sedlmair, Deriving Gaussian fatigue test spectra from measured non Gaussian service spectra, Procedia Eng. 101 (2015) 543–551, http://dx.doi.org/10.1016/j.proeng.2015.02.065, 3rd International Conference on Material and Component Performance under Variable Amplitude Loading, VAL 2015, Editors J. Papuga and M. Ruzicka.
[30] G. Sui, Y. Zhang, Response spectrum method for fatigue damage assessment of mechanical systems, Int. J. Fatigue 166 (2023) 107278, http://dx.doi.org/10.1016/j.ijfatigue.2022.107278.
[31] S. Voormeeren, D. de Klerk, D. Rixen, Uncertainty quantification in experimental frequency based substructuring, Mech. Syst. Signal Process. 24 (1) (2010) 106–118, http://dx.doi.org/10.1016/j.ymssp.2009.01.016.
[32] P. Wagner, A.P. Huesmann, M.V. van der Seijs, Application of dynamic substructuring in NVH design of electric drivetrains, in: Proceedings of the ISMA2020 Including USD2020 - International Conference on Noise and Vibration Engineering, Leuven, Belgium, September 7-9, KU Leuven, 2020, pp. 3365–3382, URL https://past.isma-isaac.be/downloads/isma2020/proceedings/Contribution_369_proceeding_3.pdf, Vehicle noise and vibration (NVH), paper ID 369.
[33] M. Haeussler, S. Klaassen, D. Rixen, Experimental twelve degree of freedom rubber isolator models for use in substructuring assemblies, J. Sound Vib. 474 (2020) 115253, http://dx.doi.org/10.1016/j.jsv.2020.115253.
[34] M. Pogacar, D. Ocepek, F. Trainotti, G. Cepon, M. Boltezar, System equivalent model mixing: A modal domain formulation, Mech. Syst. Signal Process. 177 (2022) 109239, http://dx.doi.org/10.1016/j.ymssp.2022.109239.
[35] H. Van der Auweraer, P. Mas, P. Peeters, K. Janssens, A. Vecchio, Modal and path contribution models from in-operation data: Review and new approaches, Shock Vib. 15 (2008) http://dx.doi.org/10.1155/2008/632312.
[36] P. Gajdatsy, K. Janssens, W. Desmet, H. Van der Auweraer, Application of the transmissibility concept in transfer path analysis, Mech. Syst. Signal Process. 24 (7) (2010) 1963–1976, http://dx.doi.org/10.1016/j.ymssp.2010.05.008, Special Issue: ISMA 2010.
[37] D. de Klerk, D. Rixen, Component transfer path analysis method with compensation for test bench dynamics, Mech. Syst. Signal Process. 24 (6) (2010) 1693–1710, http://dx.doi.org/10.1016/j.ymssp.2010.01.006.
[38] M.V. van der Seijs, D. de Klerk, D.J. Rixen, General framework for transfer path analysis: History, theory and classification of techniques, Mech. Syst. Signal Process. 68–69 (2016) 217–244, http://dx.doi.org/10.1016/j.ymssp.2015.08.004.

[39] R. Cumbo, T. Tamarozzi, K. Janssens, W. Desmet, Kalman-based load identification and full-field estimation analysis on industrial test case, Mech. Syst. Signal Process. 117 (2019) 771–785, http://dx.doi.org/10.1016/j.ymssp.2018.08.045.
[40] J. Ortega Almirón, F. Bianciardi, P. Corbeels, N. Pieroni, P. Kindt, W. Desmet, Vehicle road noise prediction using component-based transfer path analysis from tire test-rig measurements on a rolling tire, J. Sound Vib. 523 (2022) 116694, http://dx.doi.org/10.1016/j.jsv.2021.116694.
[41] D. Vaes, J. Swevers, P. Sas, Experimental validation of different MIMO-feedback controller design methods, Control Eng. Pract. 13 (11) (2005) 1439–1451, http://dx.doi.org/10.1016/j.conengprac.2004.12.013.
[42] U. Musella, G. D'Elia, S. Manzato, B. Peeters, P. Guillaume, F. Marulo, Analyses of target definition processes for MIMO random vibration control tests, in: N. Dervilis (Ed.), Special Topics in Structural Dynamics, Volume 6, Springer International Publishing, Cham, 2017, pp. 135–148, http://dx.doi.org/10.1007/978-3-319-53841-9_12.
[43] C. Schumann, M. Allen, M. Tuman, W. DeLima, E. Dodgen, Transmission simulator based MIMO response reconstruction, Exp. Tech. 46 (2022) 287–297, http://dx.doi.org/10.1007/s40799-021-00454-4.
[44] P.K. Rastogi, Optical Measurement Techniques and Applications, Artech House, Inc., Nordwood, MA 02062, U.S.A., 1997.
[45] T. Kreis, Handbook of Holographic Interferometry, Wiley-VCH, Berlin, Germany, 2004, http://dx.doi.org/10.1002/3527604154.
[46] H. Van der Auweraer, B. Dierckx, C. Haberstok, R. Freymann, et al., Structural modelling of car panels using holographic modal analysis, in: Proc. of the 1999 Noise and Vibration Conference, Traverse City (MI), USA, Vol. 3, 1999, pp. 1495–1506, http://dx.doi.org/10.4271/1999-01-1849, SAE P-342.
[47] H. Van der Auweraer, H. Steinbichler, C. Haberstok, R. Freymann, D. Storer, Integration of pulsed-laser ESPI with spatial domain modal analysis: results from the SALOME project, in: Proc. of the 4th International Conference on Vibration Measurements By Laser Techniques: Advances and Applications, Vol. 4072, SPIE, 2000, pp. 313–322, http://dx.doi.org/10.1117/12.386741.
[48] H. Van der Auweraer, H. Steinbichler, C. Haberstok, R. Freymann, D. Storer, V. Linet, Industrial applications of pulsed-laser ESPI vibration analysis, in: Proc. of the XIX IMAC, Kissimmee, FL, USA, SEM, 2001, pp. 490–496, URL https://www.researchgate.net/publication/238246330_Industrial_Applications_of_Pulsed-Laser_ESPI_Vibration_Analysis.
[49] H. Van der Auweraer, H. Steinbichler, S. Vanlanduit, C. Haberstok, R. Freymann, D. Storer, V. Linet, Application of stroboscopic and pulsed-ESPI to modal analysis problems, Meas. Sci. Technol. 13 (2002) 451–463, http://dx.doi.org/10.1088/0957-0233/13/4/305.
[50] A. Zanarini, Broad frequency band full field measurements for advanced applications: Point-wise comparisons between optical technologies, Mech. Syst. Signal Process. 98 (2018) 968–999, http://dx.doi.org/10.1016/j.ymssp.2017.05.035.
[51] A. Zanarini, Competing optical instruments for the estimation of Full Field FRFs, Measurement 140 (2019) 100–119, http://dx.doi.org/10.1016/j.measurement.2018.12.017.
[52] H. Lopes, J.V. Araújo dos Santos, P. Moreno-García, Evaluation of noise in measurements with speckle shearography, Mech. Syst. Signal Process. 118 (2019) 259–276, http://dx.doi.org/10.1016/j.ymssp.2018.08.042.
[53] J. Baqersad, P. Poozesh, C. Niezrecki, P. Avitabile, Photogrammetry and optical methods in structural dynamics – A review, Mech. Syst. Signal Process. 86 (2017) 17–34, http://dx.doi.org/10.1016/j.ymssp.2016.02.011, Full-field, non-contact vibration measurement methods: comparisons and applications.
[54] W. Wang, J.E. Mottershead, A. Ihle, T. Siebert, H.R. Schubach, Finite element model updating from full-field vibration measurement using digital image correlation, J. Sound Vib. 330 (8) (2011) 1599–1620, http://dx.doi.org/10.1016/j.jsv.2010.10.036.
[55] W. Wang, J. Mottershead, T. Siebert, A. Pipino, Frequency response functions of shape features from full-field vibration measurements using digital image correlation, Mech. Syst. Signal Process. 28 (2011) 333–347, http://dx.doi.org/10.1016/j.ymssp.2011.11.023, Elsevier Science Ltd.
[56] B. LeBlanc, C. Niezrecki, P. Avitabile, J. Sherwood, J. Chen, Surface stitching of a wind turbine blade using digital image correlation, in: R. Allemang, J. De Clerck, C. Niezrecki, J. Blough (Eds.), Topics in Modal Analysis II, Volume 6, Springer New York, New York, NY, 2012, pp. 277–284, http://dx.doi.org/10.1007/978-1-4614-2419-2_27.
[57] D.A. Ehrhardt, M.S. Allen, S. Yang, T.J. Beberniss, Full-field linear and nonlinear measurements using Continuous-Scan Laser Doppler Vibrometry and high speed three-dimensional Digital Image Correlation, Mech. Syst. Signal Process. 86 (Part B) (2017) 82–97, http://dx.doi.org/10.1016/j.ymssp.2015.12.003.
[58] A. Zanarini, On the estimation of frequency response functions, dynamic rotational degrees of freedom and strain maps from different full field optical techniques, in: Proceedings of the ISMA2014 Including USD2014 - International Conference on Noise and Vibration Engineering, Leuven, Belgium, September 15-17, KU Leuven, 2014, pp. 1177–1192, URL http://past.isma-isaac.be/downloads/isma2014/papers/isma2014_0676.pdf, Dynamic testing: methods and instrumentation, paper ID676.
[59] A. Zanarini, On the role of spatial resolution in advanced vibration measurements for operational modal analysis and model updating, in: Proceedings of the ISMA2014 Including USD2014 - International Conference on Noise and Vibration Engineering, Leuven, Belgium, September 15-17, KU Leuven, 2014, pp. 3397–3410, URL http://past.isma-isaac.be/downloads/isma2014/papers/isma2014_0678.pdf, Operational modal analysis, paper ID678.
[60] A. Zanarini, Full field optical measurements in experimental modal analysis and model updating, J. Sound Vib. 442 (2019) 817–842, http://dx.doi.org/10.1016/j.jsv.2018.09.048.
[61] A. Zanarini, On the making of precise comparisons with optical full field technologies in NVH, in: ISMA2020 Including USD2020 - International Conference on Noise and Vibration Engineering, Leuven, Belgium, September 7-9, KU Leuven, 2020, pp. 2293–2308, URL https://past.isma-isaac.be/downloads/isma2020/proceedings/Contribution_695_proceeding_3.pdf, Optical methods and computer vision for vibration engineering, paper ID 695.
[62] A. Zanarini, On the exploitation of multiple 3D full-field pulsed ESPI measurements in damage location assessment, Procedia Struct. Integr. 37 (2022) 517–524, http://dx.doi.org/10.1016/j.prostr.2022.01.117, paper ID 104, ICSI 2021 The 4th International Conference on Structural Integrity.
[63] A. Zanarini, On the use of full-field receptances in inverse vibro-acoustics for airborne structural dynamics, Procedia Struct. Integr. 54C (2024) 107–114, http://dx.doi.org/10.1016/j.prostr.2024.01.062, paper ID 023@ICSI2023 The 5th International Conference on Structural Integrity, 28 August - 1 September, 2023.
[64] A. Zanarini, On the approximation of sound radiation by means of experiment-based optical full-field receptances, in: ISMA2022 Including USD2022 - International Conference on Noise and Vibration Engineering, Leuven, Belgium, September 12-14, KU Leuven, 2022, pp. 2735–2749, URL https://past.isma-isaac.be/downloads/isma2022/proceedings/Contribution_207_proceeding_3.pdf, paper ID 207 in Vol. Optical Methods.
[65] A. Zanarini, Experiment-based optical full-field receptances in the approximation of sound radiation from a vibrating plate, in: IMAC XLI - International Modal Analysis Conference - Keeping IMAC Weird: Traditional and Non-Traditional Applications of Structural Dynamics, Austin (Texas), USA, Springer Nature Switzerland AG & SEM Society for Experimental Mechanics, 2023, pp. 1–13, http://dx.doi.org/10.1007/978-3-031-34910-2_4, paper ID 14650 - chapter 4, in J. Baqersad, D. Di Maio (eds.), Computer Vision & Laser Vibrometry, Volume 6, Conference Proceedings of the Society for Experimental Mechanics Series.
[66] A. Zanarini, On the influence of scattered errors over full-field receptances in the Rayleigh integral approximation of sound radiation from a vibrating plate, Acoustics 5 (2023) 948–986, http://dx.doi.org/10.3390/acoustics5040055.
[67] W. Liu, D. Ewins, The importance assessment of RDOF in FRF coupling analysis, in: Proceedings of the IMAC 17th Conference, Kissimmee, Florida, 1999, pp. 1481–1487, URL https://citeseerx.ist.psu.edu/document?repid=rep1&type=pdf&doi=c44ebc7b37f462e47b44aee1acb1f9de704e92d6, Society for Experimental Mechanics (SEM).
[68] Research network, QUATTRO Brite-Euram Project No: BE 97-4184, Tech. Rep., European Commision Research Framework Programs, 1998.
[69] M. Friswell, J.E. Mottershead, Finite element model updating in structural dynamics, in: Solid Mechanics and Its Applications, Kuwler Academic Publishers, Springer Netherlands, 1995, p. 292, URL https://link.springer.com/book/10.1007/978-94-015-8508-8.
[70] W.H. Press, S.A. Teukolsky, W.T. Vetterling, B.P. Flannery, Numerical Recipes in C: The Art of Scientific Computing, second ed., Cambridge Univ. Press, England, 1992, URL http://numerical.recipes.

[71] J. Araújo dos Santos, H. Lopes, Savitzky-golay smoothing and differentiation filters for damage identification in plates, Procedia Struct. Integr. 54 (2024) 575–584, http://dx.doi.org/10.1016/j.prostr.2024.01.121, International Conference on Structural Integrity 2023 (ICSI 2023).
[72] F. Tisseur, K. Meerbergen, The quadratic eigenvalue problem, SIAM Rev. 43 (2) (2001) 235–286, URL http://www.jstor.org/stable/3649752.
[73] L. Starek, D. Inman, Symmetric inverse eigenvalue vibration problem and its application, Mech. Syst. Signal Process. 15 (1) (2001) 11–29, http://dx.doi.org/10.1006/mssp.2000.1349.
[74] C. Hoen, V.A. As, An engineering interpretation of the complex eigensolution of linear dynamic systems, in: Proceedings of International Modal Analysis Conference XXIII, SEM, Society of Experimental Mechanics, 2005, pp. 1–9, URL https://www.svibs.com/wp-content/uploads/2023/11/2005_16.pdf, Orlando - Florida, USA, January 31 - February 5.
[75] R. von Mises, Mechanik der festen Koerper im plastisch- deformablen Zustand, in: Nachrichten Von Der Gesellschaft Der Wissenschaften Zu Goettingen, Mathematisch-Physikalische Klasse, Vol. 1913, 1913, pp. 582–592, URL http://eudml.org/doc/58894.
[76] D. Benasciutti, Some analytical expressions to measure the accuracy of the “equivalent von Mises stress” in vibration multiaxial fatigue, J. Sound Vib. 333 (18) (2014) 4326–4340, http://dx.doi.org/10.1016/j.jsv.2014.04.047.
[77] D. Benasciutti, An analytical approach to measure the accuracy of various definitions of the “equivalent von Mises stress” in vibration multiaxial fatigue, in: Proceedings of the ICoEV2015 International Conference on Engineering Vibration, Ljubljana, Slovenia, September 7-10, Univ. Ljubljana & IFToMM, 2015, pp. 743–752.
[78] A. Carpinteri, A. Spagnoli, S. Vantadori, Reformulation in the frequency domain of a critical plane-based multiaxial fatigue criterion, Int. J. Fatigue 67 (Supplement C) (2014) 55–61, http://dx.doi.org/10.1016/j.ijfatigue.2014.01.008, Multiaxial Fatigue 2013.
[79] C. Braccesi, F. Cianetti, L. Tomassini, Fast evaluation of stress state spectral moments, Int. J. Mech. Sci. 127 (Supplement C) (2017) 4–9, http://dx.doi.org/10.1016/j.ijmecsci.2016.11.007, Special Issue from International Conference on Engineering Vibration - ICoEV 2015.
[80] J. Papuga, M. Nesládek, A. Hasse, E. Cízová, L. Suchý, Benchmarking newer multiaxial fatigue strength criteria on data sets of various sizes, Metals 12 (2) (2022) 289:1–30, http://dx.doi.org/10.3390/met12020289.
[81] C. Braccesi, F. Cianetti, G. Lori, D. Pioli, An equivalent uniaxial stress process for fatigue life estimation of mechanical components under multiaxial stress conditions, Int. J. Fatigue 30 (8) (2008) 1479–1497, http://dx.doi.org/10.1016/j.ijfatigue.2007.09.011.
[82] A. Cristofori, D. Benasciutti, R. Tovo, A stress invariant based spectral method to estimate fatigue life under multiaxial random loading, Int. J. Fatigue 33 (7) (2011) 887–899, http://dx.doi.org/10.1016/j.ijfatigue.2011.01.013.
[83] M. Mršnik, J. Slavič, M. Boltežar, Frequency-domain methods for a vibration-fatigue-life estimation – Application to real data, Int. J. Fatigue 47 (Supplement C) (2013) 8–17, http://dx.doi.org/10.1016/j.ijfatigue.2012.07.005.
[84] C. Braccesi, F. Cianetti, G. Lori, D. Pioli, Evaluation of mechanical component fatigue behavior under random loads: Indirect frequency domain method, Int. J. Fatigue 61 (Supplement C) (2014) 141–150, http://dx.doi.org/10.1016/j.ijfatigue.2013.11.017.
[85] C. Braccesi, F. Cianetti, G. Lori, D. Pioli, Random multiaxial fatigue: A comparative analysis among selected frequency and time domain fatigue evaluation methods, Int. J. Fatigue 74 (Supplement C) (2015) 107–118, http://dx.doi.org/10.1016/j.ijfatigue.2015.01.003.
[86] C. Braccesi, F. Cianetti, L. Tomassini, Random fatigue. A new frequency domain criterion for the damage evaluation of mechanical components, Int. J. Fatigue 70 (Supplement C) (2015) 417–427, http://dx.doi.org/10.1016/j.ijfatigue.2014.07.005.
[87] D. Benasciutti, F. Sherratt, A. Cristofori, Recent developments in frequency domain multi-axial fatigue analysis, Int. J. Fatigue 91 (Part 2) (2016) 397–413, http://dx.doi.org/10.1016/j.ijfatigue.2016.04.012, Variable Amplitude Loading.
[88] C. Braccesi, F. Cianetti, L. Tomassini, An innovative modal approach for frequency domain stress recovery and fatigue damage evaluation, Int. J. Fatigue 91 (Part 2) (2016) 382–396, http://dx.doi.org/10.1016/j.ijfatigue.2016.02.028, Variable Amplitude Loading.
[89] J. Papuga, M. Margetin, V. Chmelko, Various parameters of the multiaxial variable amplitude loading and their effect on fatigue life and fatigue life computation, Fatigue Fract. Eng. Mater. Struct. 44 (10) (2021) 2890–2912, http://dx.doi.org/10.1111/ffe.13560.
[90] A. Zorman, J. Slavič, M. Boltežar, Vibration fatigue by spectral methods—A review with open-source support, Mech. Syst. Signal Process. 190 (2023) 110149, http://dx.doi.org/10.1016/j.ymssp.2023.110149.
[91] M. Aimé, A. Banvillet, L. Khalij, E. Pagnacco, E. Chatelet, R. Dufour, A framework proposal for new multiaxial fatigue damage and extreme response spectra in random vibrations frequency analysis, Mech. Syst. Signal Process. 213 (2024) 111338, http://dx.doi.org/10.1016/j.ymssp.2024.111338.
[92] J.S. Bendat, A.G. Piersol, Random Data: Analysis and Measurement Procedures, third ed., John Wiley & Sons Inc, 2000.
[93] B.V. Farahani, F. Direito, P.J. Sousa, F.Q. Melo, P.J. Tavares, V. Infante, P.M. Moreira, Advancement on optical methods in stress dead-zone characterisation and SIF evaluation, Eng. Fail. Anal. 140 (2022) 106493, http://dx.doi.org/10.1016/j.engfailanal.2022.106493.
[94] B.V. Farahani, F. Direito, P.J. Sousa, P.J. Tavares, V. Infante, P.P. Moreira, Crack tip monitoring by multiscale optical experimental techniques, Int. J. Fatigue 155 (2022) 106610, http://dx.doi.org/10.1016/j.ijfatigue.2021.106610.
[95] J. Araújo dos Santos, H. Lopes, M. Vaz, C. Mota Soares, C. Mota Soares, M. de Freitas, Damage localization in laminated composite plates using mode shapes measured by pulsed TV holography, Compos. Struct. 76 (3) (2006) 272–281, http://dx.doi.org/10.1016/j.compstruct.2006.06.034, US Air Force Workshop Health Assessment of Composite Structures.